Energy 189 (2019) 116131

Contents lists available at ScienceDirect

Energy

journal homepage: www.elsevier.com/locate/energy

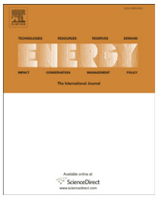

Active flow control for power enhancement of vertical axis wind turbines: Leading-edge slot suction

Abdolrahim Rezaeiha [a, *], Hamid Montazeri [a, b], Bert Blocken [a, b]

[a] *Eindhoven University of Technology, Eindhoven, the Netherlands*
[b] *KU Leuven, Leuven, Belgium*

ARTICLE INFO

Article history:
Received 17 July 2019
Received in revised form
3 September 2019
Accepted 13 September 2019
Available online 14 September 2019

Keywords:
Active separation control
Dynamic stall control
Characterization
Optimization
VAWT
Urban and offshore wind energy

ABSTRACT

Vertical axis wind turbines (VAWTs) suffer from a poor power performance at low tip speed ratios, where their blade aerodynamics are dominated by unsteady separation and dynamic stall. Therefore, to enhance their aerodynamic performance, separation control is highly desired. The present study intends to suppress the flow separation on VAWTs using boundary layer suction through a slot located near the blade leading edge. High-fidelity computational fluid dynamics simulations extensively validated with experiments are employed. A characterization of the impact of the suction amplitude, $0.5\% \leq A_S \leq 10\%$, and the suction location, $8.5 \leq X_S/c \leq 28.5$, is performed. The dependency of the obtained power gain on operating conditions, i.e. tip speed ratio, $2.5 \leq \lambda \leq 3.5$, Reynolds number, $0.51 \times 10^5 \leq Re_c \leq 2.78 \times 10^5$, and turbulence intensity, $1\% \leq TI \leq 25\%$, is studied. The results show that applying suction along the chordwise extent of the laminar separation bubble (LSB) can prevent its bursting, eliminate/postpone its formation, avoid the formation of the dynamic stall vortex and trailing-edge roll-up vortex, and delay the incipient trailing-edge separation. This will significantly increase the blade lift force, decrease the drag force, delay the stall angle and suppress the aerodynamic load fluctuations. For the reference turbine and for $A_S = 0.5\%$ and $X_S/c = 8.5\%$, the power coefficient at λ of 2.5, 3.0 and 3.5 is enhanced by 247%, 83% and 24%, respectively. The suction location is critical while a minimum amplitude, e.g. $A_S = 0.5\%$, suffices. The optimal suction location is insensitive to TI, weakly sensitive to λ while comparatively more sensitive to Re_c.

© 2019 The Authors. Published by Elsevier Ltd. This is an open access article under the CC BY license (http://creativecommons.org/licenses/by/4.0/).

1. Introduction

Vertical axis wind turbines (VAWTs) are promising candidates for floating offshore windfarms as well as for wind energy harvesting in urban areas, due to a number of specific advantages, especially their omni-directionality, scalability and low noise [1–5]. However, their aerodynamic performance, expressed in terms of power coefficient C_P, is currently not comparable with horizontal axis wind turbines (HAWTs) [2,6]. Therefore, improvement of the aerodynamic performance of VAWTs can make them competitive with HAWTs and render them ideal options for wind energy harvesting in the aforementioned locations.

The comparatively low aerodynamic performance of VAWTs could be attributed to their complex unsteady aerodynamics, which has not yet been comprehensively elucidated. The blade aerodynamics of VAWTs are dominated by large excursions of the angle of attack and the relative velocity as well as rotational flow effects. Simultaneous occurrence of several flow phenomena, namely dynamic stall, blade-vortex and vortex-vortex interactions, flow rotational and curvature effects, greatly complicate the blade aerodynamics of VAWTs, where such complexity increases at lower tip speed ratios [7–14].

Variations of the angle of attack on VAWT blades at low tip speed ratio can significantly exceed the stall angle and, therefore, result in occurrence of deep dynamic stall on the blades, where the flow separation can considerably dominate the blade aerodynamics and adversely influence the turbine power performance [14–21].

Therefore, suppression of the unsteady separation and dynamic stall on VAWTs is highly desired [22–25] and can be an effective means toward enhancing their aerodynamic performance and bringing their power coefficient C_P closer to that of HAWTs.

Flow control has emerged as a remedy to affect flow separation. In general, flow control is defined as local manipulation of flow features towards desired characteristics [26–28] and it has been

---

* Corresponding author.
E-mail address: a.rezaeiha@tue.nl (A. Rezaeiha).

https://doi.org/10.1016/j.energy.2019.116131
0360-5442/© 2019 The Authors. Published by Elsevier Ltd. This is an open access article under the CC BY license (http://creativecommons.org/licenses/by/4.0/).

Nomenclature

A	Turbine swept area, $h \cdot d$ [m^2]
A_S	Suction amplitude, $\frac{V_w}{U_\infty}$ [%]
c	Blade chord length [m]
C_d	Sectional drag coefficient, $D/(qA)$ [−]
C_f	Skin friction coefficient [−]
C_{Fx}	Instantaneous streamwise force coefficient, $F_x/(qA)$ [−]
C_l	Sectional lift coefficient, $L/(qA)$ [−]
C_m	Instantaneous moment coefficient, $M/(qAR)$ [−]
C_P	Turbine power coefficient, $P/(qAU_\infty)$ [−]
C_T	Turbine thrust coefficient, $T/(qA)$ [−]
CoP	Pressure coefficient, P_g/q [−]
d	Turbine diameter [m]
D	Drag force [N]
F_x	Instantaneous streamwise force [N]
h	Turbine height [m]
k	Turbulent kinetic energy [m^2/s^2]
K	Reduced frequency, $\Omega c/(2V_{rel}) \approx c/2R$ [−]
L	Lift force [N]
M	Instantaneous turbine moment [N.m]
n	Number of blades [−]
P	Turbine average power [W]
P_g	Static gauge pressure [Pa]
q	Dynamic pressure [Pa]
R	Turbine radius [m]
Re_c	Chord-based Reynolds number, $cU_\infty\sqrt{1+\lambda^2}/\nu$ [−]
Re_θ	Momentum-thickness Reynolds number [−]
t	Time [s]
T	Turbine average thrust force [N]
TI	Approach-flow (i.e. inlet) total turbulence intensity [%]
TI_i	Incident-flow total turbulence intensity [%]
U_∞	Freestream velocity [m/s]
u	Instantaneous streamwise velocity [m/s]
v	Instantaneous lateral velocity [m/s]
$V_{rel,n}$	Relative mean velocity normalized with $U_\infty\sqrt{1+\lambda^2}$ [−]
$V_{tan,n}$	Instantaneous dimensionless tangential velocity, $(u\cos(\theta)+v\sin(\theta))/U_\infty$ [−]
V_W	Suction velocity [m/s]
W	Width of suction slot [%]
X_S	Center position of suction slot measured along the blade chord [m]
$X_{S,1}$	Start position of suction slot measured along the blade chord [m]
$X_{S,2}$	End position of suction slot measured along the blade chord [m]
X/c	Dimensionless chordwise position along the blade [−]
α	Experienced angle of attack [°]
γ	Intermittency [−]
θ	Azimuth angle [°]
θ_0	Unperturbed boundary layer momentum thickness [m]
λ	Tip speed ratio, $R\Omega/U_\infty$ [−]
ν	Kinematic viscosity of air [m^2/s]
σ	Solidity, nc/d [−]
ω	Specific dissipation rate [1/s]
ω_z	z-vorticity [1/s]
Ω	Turbine rotational speed [rad/s]

employed with aims such as flow separation control, circulation and load control, transition control, drag reduction, heat transfer/mixing enhancement and noise suppression [29–33]. Flow control actuators are categorized as passive (not requiring energy input, e.g. Gurney flap [24,34–37]) and active (requiring energy input, e.g. suction and blowing [38–41]) devices, where both have already been investigated/employed for numerous applications, such as aircrafts, helicopters, cars, wind turbines and turbomachinery [25,42–45].

Boundary layer suction is a classic flow control method where the near-wall fluid is sucked through porous surfaces or slots in order to reshape the boundary layer velocity profile. Boundary layer suction is normally employed to control separation and transition. Boundary layer suction was introduced and applied by Prandtl [46] to suppress flow separation on a circular cylinder. Since then, this method has been investigated, developed and employed for different applications including aircrafts, helicopters, cars and wind turbines [47–53].

Recently, the application of flow control devices on VAWTs has received attention, however with a focus on passive flow control mechanisms. The impact of leading-edge serrations on power performance of VAWTs has been numerically studied by Wang et al. [54,55], where a maximum improvement of 18.7% in turbine efficiency in terms of the power coefficient C_P at the low tip speed ratio of $\lambda = 2.0$ has been achieved. Gurney flaps have also been numerically studied for VAWTs by Zhu et al. [56] and Bianchini et al. [57], where a maximum power gain of about 23% in C_P has been achieved for $\lambda = 3.3$. Due to the inherently unsteady physics of VAWTs, passive measures are known to have limited power gain for VAWTs [58–60] and active flow control methods could be much more promising as their performance can be adapted to the local operating conditions of the turbine. Research on active flow control for VAWTs is very limited [61–64] and, to the best of our knowledge, the influence of boundary layer suction on the aerodynamic performance of VAWTs has not yet been investigated.

In this perspective, the current study aims to provide insights on the impact of boundary layer suction through a leading-edge slot on the suppression of unsteady separation and dynamic stall on blades of VAWTs in order to enhance their aerodynamic performance.

The objectives of the present work are as follows:

- To understand the influence of boundary layer suction on the blade aerodynamics and the turbine power performance of VAWTs at low tip speed ratios;
- To characterize the impact of suction characteristics, namely suction amplitude and location, on the blade aerodynamics and the turbine power performance of VAWTs at low tip speed ratios;
- To analyze the dependency of the turbine power gain due to suction on operational parameters, namely tip speed ratio, turbulence intensity and Reynolds number;
- To identify the optimal suction characteristics for various turbine operating conditions.

The aforementioned objectives are to be achieved using high-fidelity CFD simulations. The CFD simulations are extensively validated with different sets of experiments in four different validation studies.

The outline of the paper is as follows. The computational settings and parameters are described in Section 2. Three sets of validation studies for three different VAWTs are presented in Section 3.1. A validation study for a flat plate with slot suction in a turbulent boundary layer is presented in Section 3.2. The influence of boundary layer suction on the blade aerodynamics and the turbine power performance is analyzed in Section 4.1 and 4.2. Section 4.3 investigates the impact of suction amplitude and location. Section 5 characterizes the turbine power gain due to suction for various operational parameters, namely tip speed ration, chord-based Reynolds number and turbulence intensity. Discussion and conclusions are provided in Section 6 and 7.

2. Computational settings and parameters

2.1. Geometrical and operational characteristics

Table 1 lists the geometrical characteristics of the reference turbine, the reference operating conditions and the reference characteristics of the leading-edge slot suction. Fig. 1 illustrates a schematic of the turbine with slot suction. Note that as the focus of the study is on the impact of boundary layer suction, for the sake of computational cost, the turbine is simplified to include only one blade, no shaft and no spokes. The impact of the number of blades and the turbine shaft has been investigated previously in detail in Refs. [60,65].

The suction slot is located on the blade inner side, which during the turbine first half-revolution corresponds to the blade suction side. The suction slot is positioned near the blade leading-edge aiming to suppress the dynamic stall phenomena, which dominate the blade aerodynamics of VAWTs at low tip speed ratios [13,14,19,60,66].

2.2. Computational settings

The employed computational settings are listed in Table 2 and are based on the guidelines for accurate CFD simulations of VAWTs [19,60,67–69]. The computational domain and grid are shown in Fig. 2.

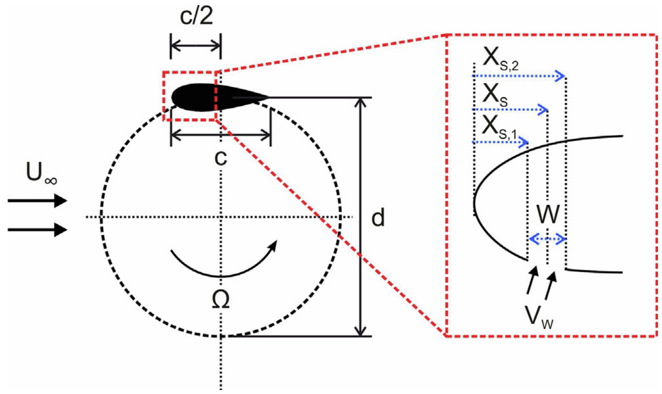

Fig. 1. Schematic (top-view) of the turbine with zoom-in on the suction slot.

2.3. Solution verification

Extensive solution verification analyses have been already performed to investigate the impact of computational settings for the CFD simulations of VAWTs [19,67–69,71]. Additional grid convergence analysis using uniformly-doubled grids and time-step sensitivity analysis performed for the VAWT with suction, see Fig. 3, show that the coarse grid with an azimuthal increment of 0.1° can be used for the rest of the study.

3. Validation studies

3.1. Vertical axis wind turbine

Three sets of validation studies have been performed for VAWTs with different geometrical and operational characteristics, where acceptable agreements between the CFD results and experimental data have been observed. The complete description of the validation studies is presented in Refs. [59,68,69] and for brevity is not repeated here.

Table 1
Geometrical characteristics of the reference turbine with suction at reference conditions.

Reference turbine	
Type	Darrieus H-type
Number of blades, n	1
Diameter, d *[m]*	1
Height, h *[m]*	1
Swept area, A *[m^2]*	1
Solidity, σ	0.06
Airfoil	NACA0018
Airfoil chord, c *[m]*	0.06
Blade aspect ratio, h/c	16.67
Location of blade-spoke connection	Half-chord, c/2
Rotation direction	Counter-clockwise
Reference operating conditions	
Freestream velocity, U_∞ *[m/s]*	9.3
Turbine rotational velocity, Ω *[rad/s]*	46.5 − 65.1
Tip speed ratio, λ	2.5 −3.5
Chord-based Reynolds number, Re_c	$1.03 \times 10^5 - 1.39 \times 10^5$
Approach-flow total turbulence intensity, TI [%]	5
Reference suction characteristics (see Fig. 2)	
Start location, $X_{S,1}/c$ *[%]*	7.33
Center location, X_S/c*[%]*	8.50
End location, $X_{S,2}/c$ *[%]*	9.83
Width, W/c *[%]*	2.5
Suction velocity, V_W *[m/s]*	0.0465 (inward)
Amplitude, A_S *[%]*	0.5

Table 2
Computational settings.

Domain (see Fig. 2a)	Two-dimensional (2D); $35d \times 20d$
Grid (see Fig. 2b–f)	366,976 quadrilateral cells; $y^{+}_{max} < 1.0$; 1100 cells along the blade cross-sectional circumference; 150 cells along the suction slot
Boundary conditions	*Inlet*: uniform mean velocity; total turbulence intensity = 5% (the incident *TI* is 3.96% due to the turbulence decay in the domain, see Refs. [68,70]; turbulence length scale = 1 m (= d); *Outlet*: zero static gauge pressure; *Side boundaries*: symmetry; *Blade walls*: no-slip; *Suction slot*: uniform inward normal velocity; laminar (Reynolds number based on $W < 200$)
Turbulence model	4-eq. transition SST
CFD approach	Incompressible unsteady Reynolds-averaged Navier-Stokes (URANS)
Solver	ANSYS Fluent v16.1
Discretization order (time and space)	2nd order
Pressure-velocity coupling scheme	SIMPLE
Azimuthal increment	0.1°
Number of turbine revolutions to reach statistical convergence	20 (presented results are at 21st revolution)

3.2. Slot suction over a flat plate with turbulent boundary layer

Due to lack of high-resolution experimental data for VAWTs with slot suction, the experiments by van der Hoeven [72] are used for validation of CFD simulations of boundary layer suction. In the experiments, the surface pressure along a flat plate with slot suction in a turbulent boundary layer was measured. The incoming flow over the flat plate was ensured to be 2D. The momentum-thickness Reynolds number ($Re_{\theta,0}$) for the unperturbed boundary layer (i.e. suction off) at the location of suction was 10,100, corresponding to a local boundary layer momentum thickness of $\theta_0 = 5.6$ mm. Description of the experiments and the computational settings are listed in Table 3. Fig. 4 illustrates a schematic of the suction slot along the flat plate and the computational grid. Note that the grid is selected based on a sensitivity analysis using a uniformly-doubled grid. The boundary conditions for the

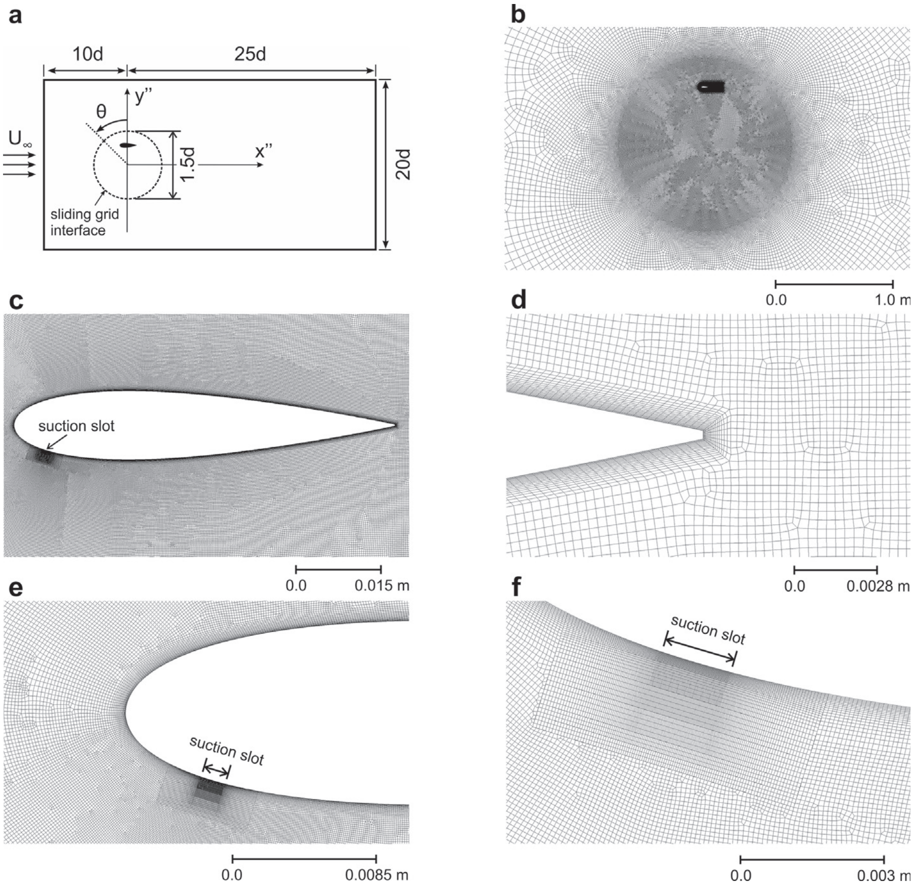

Fig. 2. (a) Schematic of computational domain (not-to-scale); (b–f) different regions of computational grid near (b) rotating core, (c) blade, (d) trailing edge, (e) leading edge, and (f) suction slot. Total cell count is 366,976.

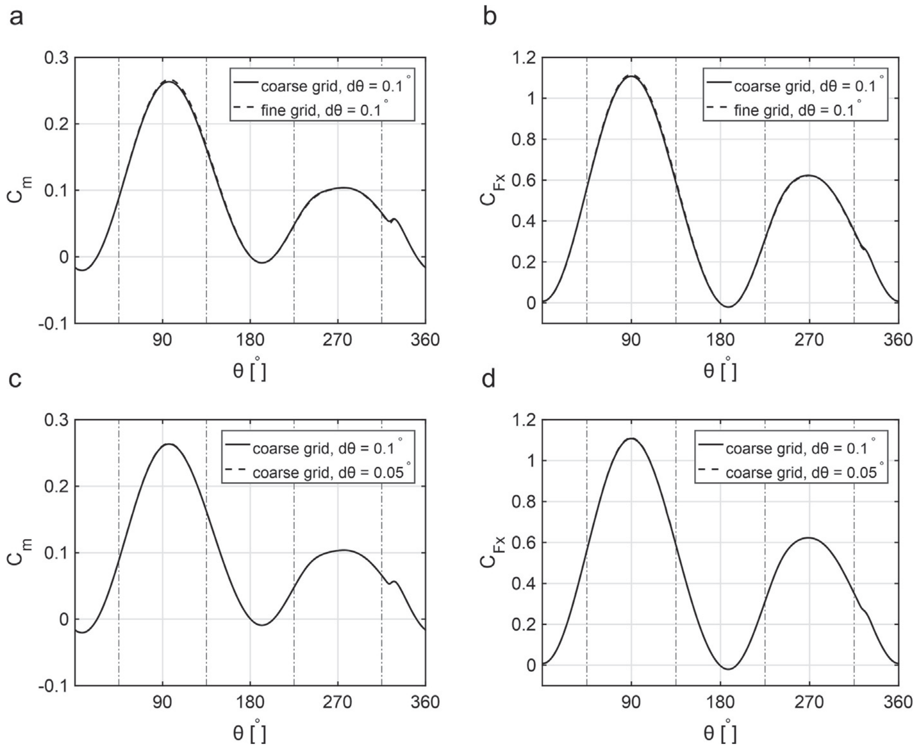

Fig. 3. Instantaneous moment and streamwise force coefficients during the last turbine revolution for the reference turbine at the reference operating conditions: (a–b) grid and (c–d) time-step sensitivity analyses.

Table 3
Description of experiment [72] and computational settings.

Experiment	
Approach-flow velocity (U_∞)	28 m/s
Streamwise turbulence intensity (I_u)	5%
Suction sot width	10 mm
Suction velocity	− 6.23 m/s
Computational settings	
Domain	Two-dimensional; 76W × 15W (suction slot is 30W from domain inlet)
Grid (see Fig. 4b and c)	70,500 quadrilateral cells; $y^+_{max} < 1.0$; 1100 cells along the blade cross-sectional circumference; 60 cells along the suction slot
Turbulence model	SST k-ω
CFD approach	Incompressible steady RANS
Solver	ANSYS Fluent v16.1
Discretization order	2nd order
Pressure-velocity coupling scheme	SIMPLE

simulations at the domain inlet, outlet, top and at the flat plate and suction slot are velocity inlet, zero static gauge pressure, symmetry, no-slip wall and velocity inlet (uniform inward). The domain inlet profiles are selected the same as the experimental data at x'/W = −30.0, given in Ref. [72].

Fig. 5 compares the CFD results with the experimental data for the surface pressure coefficient, *CoP*, along the flat plate with slot suction at $0 \leq x'/W \leq 1$, where a very good agreement is observed.

4. Influence of boundary layer suction

In this section, a detailed analysis of the impact of boundary layer suction through a slot located near the blade leading edge on the blade aerodynamics and the turbine power performance is presented. The analysis is performed for the reference turbine at the reference operating conditions, see Table 1.

In this section, the focus of the analysis is on the turbine first half-revolution, i.e. $0° \leq \theta \leq 180°$ (see Fig. 2a), because during this period the blade inner side, where the suction slot is placed, corresponds to the blade suction side. Therefore, the boundary layer suction is expected to improve the blade aerodynamics and the turbine power performance.

4.1. Blade aerodynamics

Fig. 6 shows the experienced angle of attack α and normalized relative velocity $V_{rel,n}$ during the turbine half-revolution. The method employed to calculate the experienced values of angle of attack and relative velocity from CFD results is presented in detail in Ref. [71]. Note that the presented values correspond to the reference turbine with no suction (suc. off). Nevertheless, the α and $V_{rel,n}$ values for the reference turbine with suction (suc. on) are

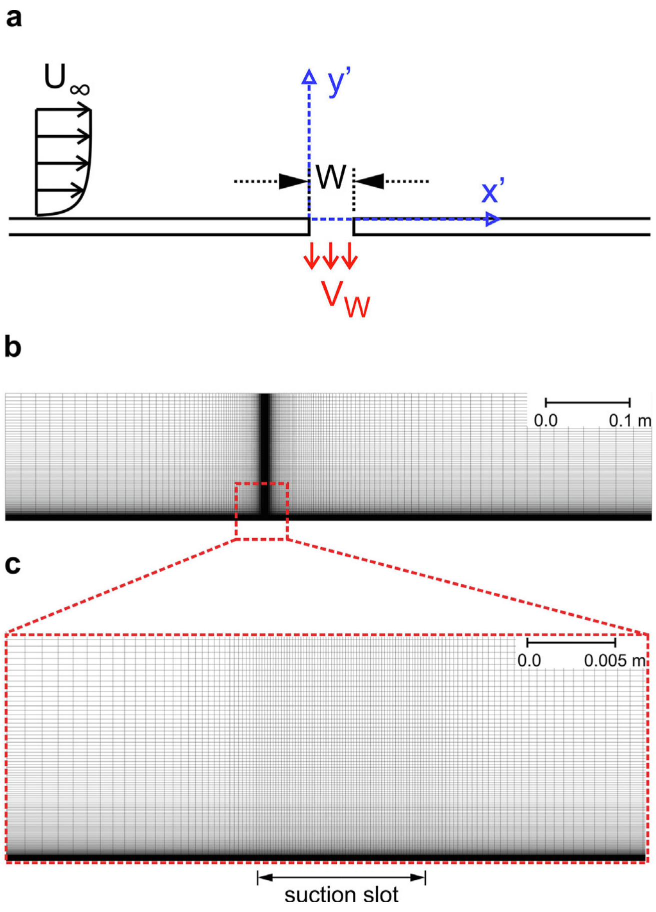

Fig. 4. (a) Schematic of the flat plate with suction slot; (b–c) computational grid. Total cell count is 70,500.

found to be overlapping.

The figure shows that for the three λ values of 2.5, 3.0 and 3.5, α exceeds the static stall angle, α_{SS}, of 14°, where α_{SS} is based on Xfoil [73] calculations for NACA0018 at $Re = 10^5$. For $\lambda = 2.5$, the maximum angle of attack, α_{max}, far exceeds α_{SS} and reaches 23.1° at $\theta = 113°$. For $\lambda = 3.0$, α_{max} reaches 18.8° at $\theta = 109°$. For $\lambda = 3.5$, α_{max} hardly exceeds α_{SS} by reaching 15.7° at $\theta = 105°$.

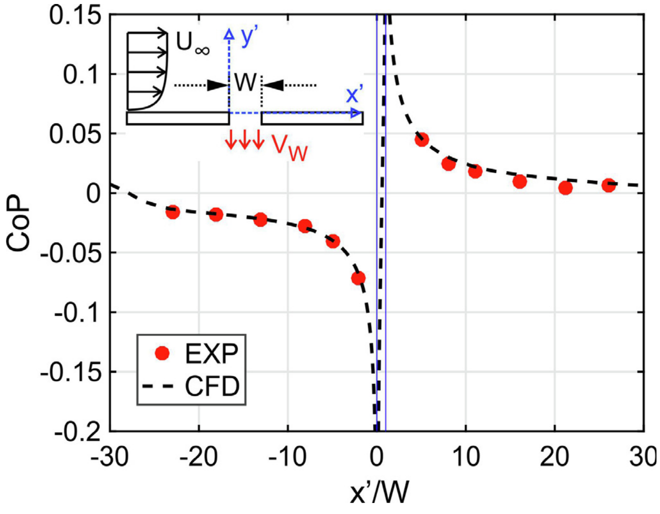

Fig. 5. The validation for flat plate with slot suction: comparison of calculated (CFD) and measured [72] surface pressure coefficient along a flat plate with slot suction, located at $0 \le x/W \le 1$, in a turbulent boundary layer, $Re_\theta = 10{,}100$.

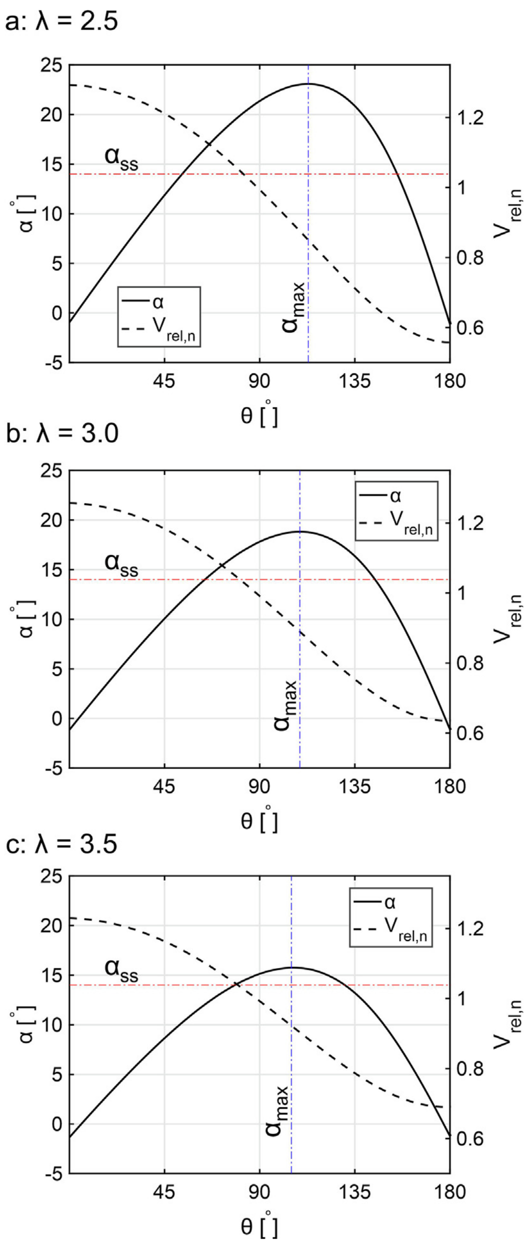

Fig. 6. Experienced angle of attack and relative mean velocity (normalized using $U_\infty\sqrt{1+\lambda^2}$) during the turbine half-revolution.

Fig. 7 presents the line plots of skin friction and surface pressure coefficients (C_f and CoP) along the blade suction side (inner side) at selected azimuthal positions prior to the shedding of laminar separation bubble (LSB). Figs. 8 and 9 present the spatiotemporal contour plots of C_f and CoP along the blade suction side (inner side) during the turbine half-revolution. The presented plots help to identify the characteristics (i.e. formation, size, growth, bursting/shedding) of the most important flow phenomena on the turbine blade, i.e. (i) laminar separation bubble (LSB): the LSB is typically recognized by a pressure plateau followed by a rapid recovery in the pressure coefficient line plots across the blade chord length, and also by negative C_f values near the leading edge, (ii) dynamic stall vortex (DSV): the DSV is recognized by a diagonal imprint of

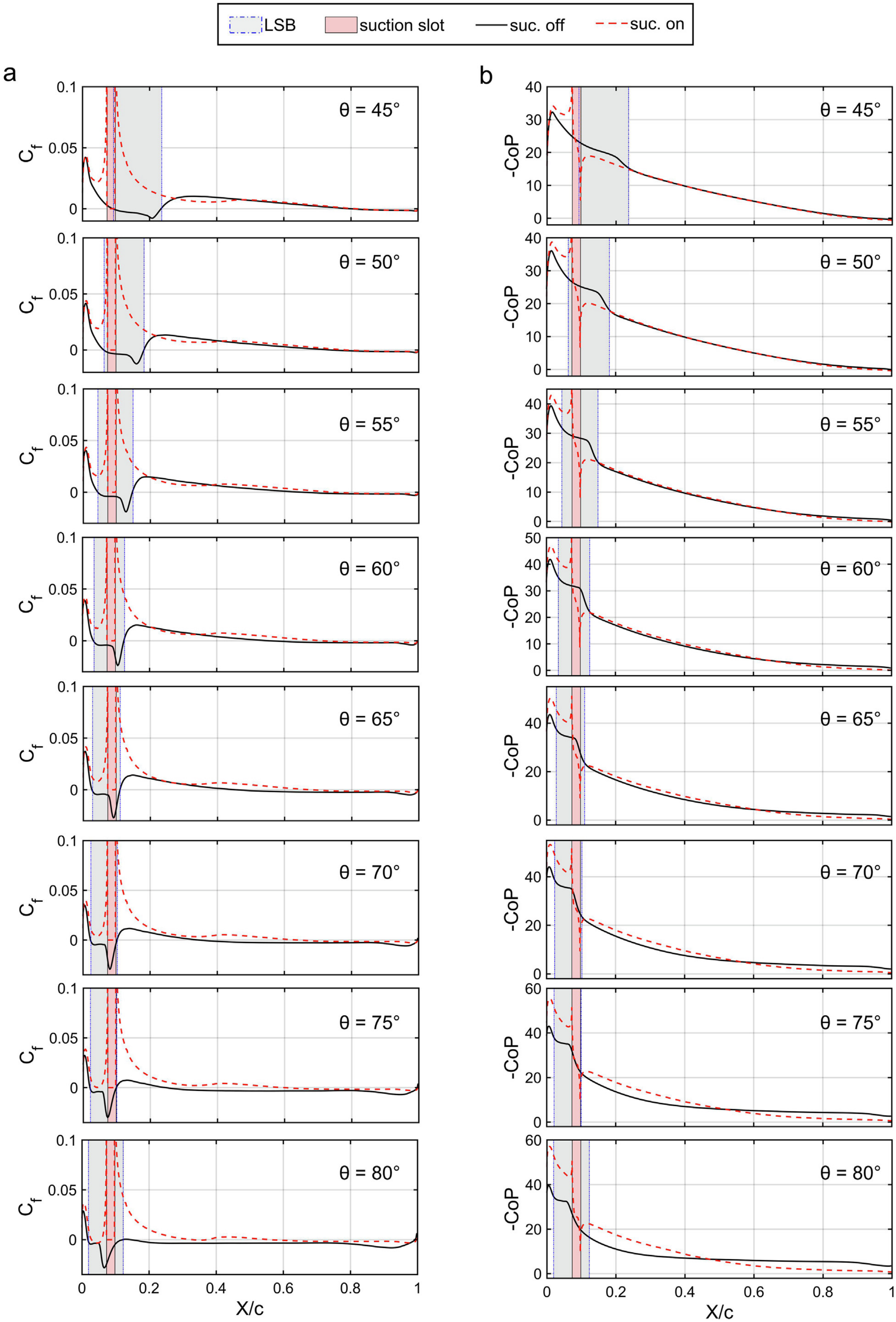

Fig. 7. Line plots of skin friction and pressure coefficients along the blade suction side at selected azimuthal positions prior to the shedding of LSB. Note that the X-axis is oriented along the chord and rotating along with the blade.

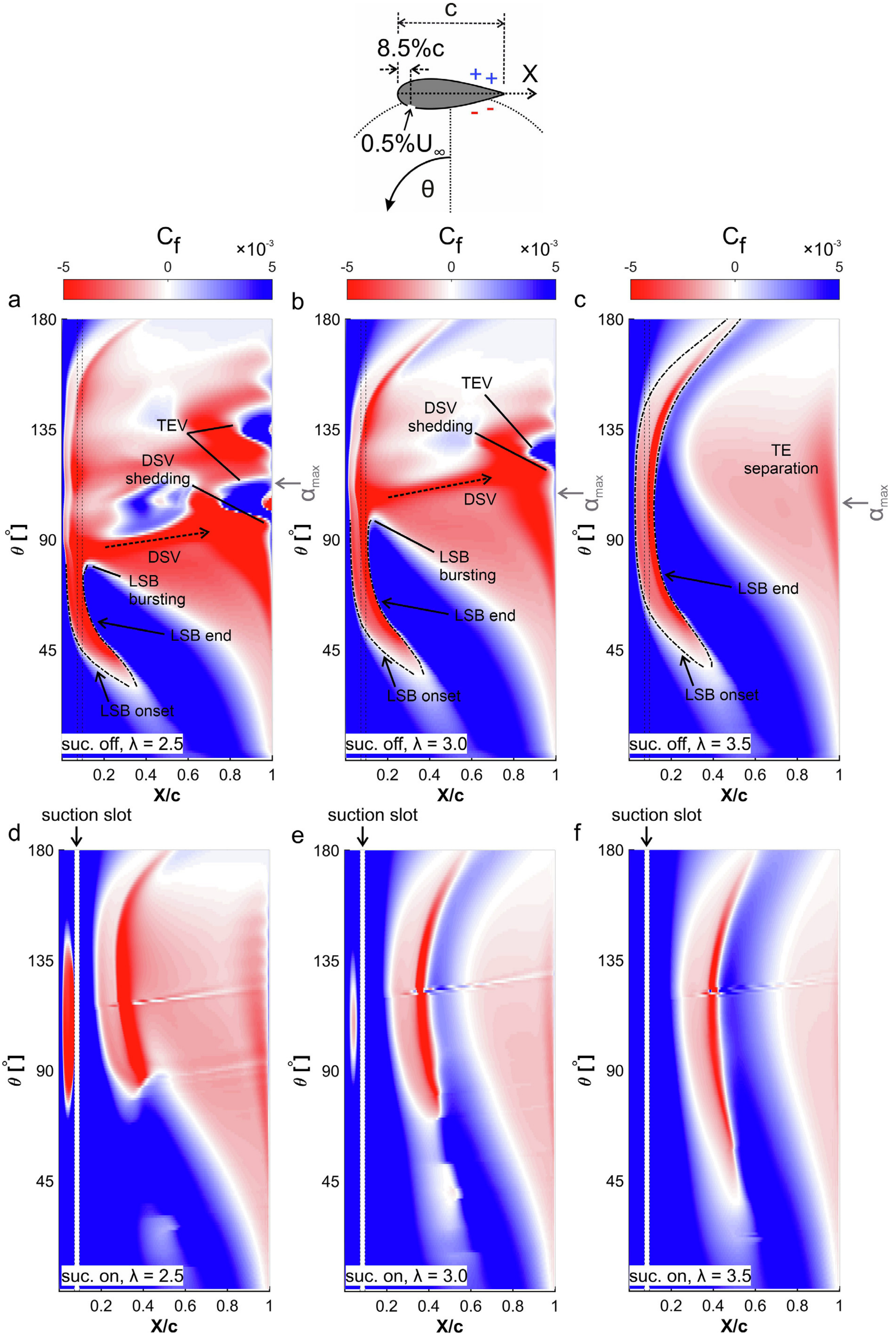

Fig. 8. Spatiotemporal contour plots of skin friction coefficient along the blade suction side (denoted with '–' sign in the schematic above) during the turbine half-revolution. LSB: laminar separation bubble; DSV: dynamic stall vortex; TE: trailing edge; TEV: trailing-edge roll-up vortex. Note that the X-axis is oriented along the chord and rotating along with the blade. The vertical dashed lines in sub-fig. a-c show the suction location.

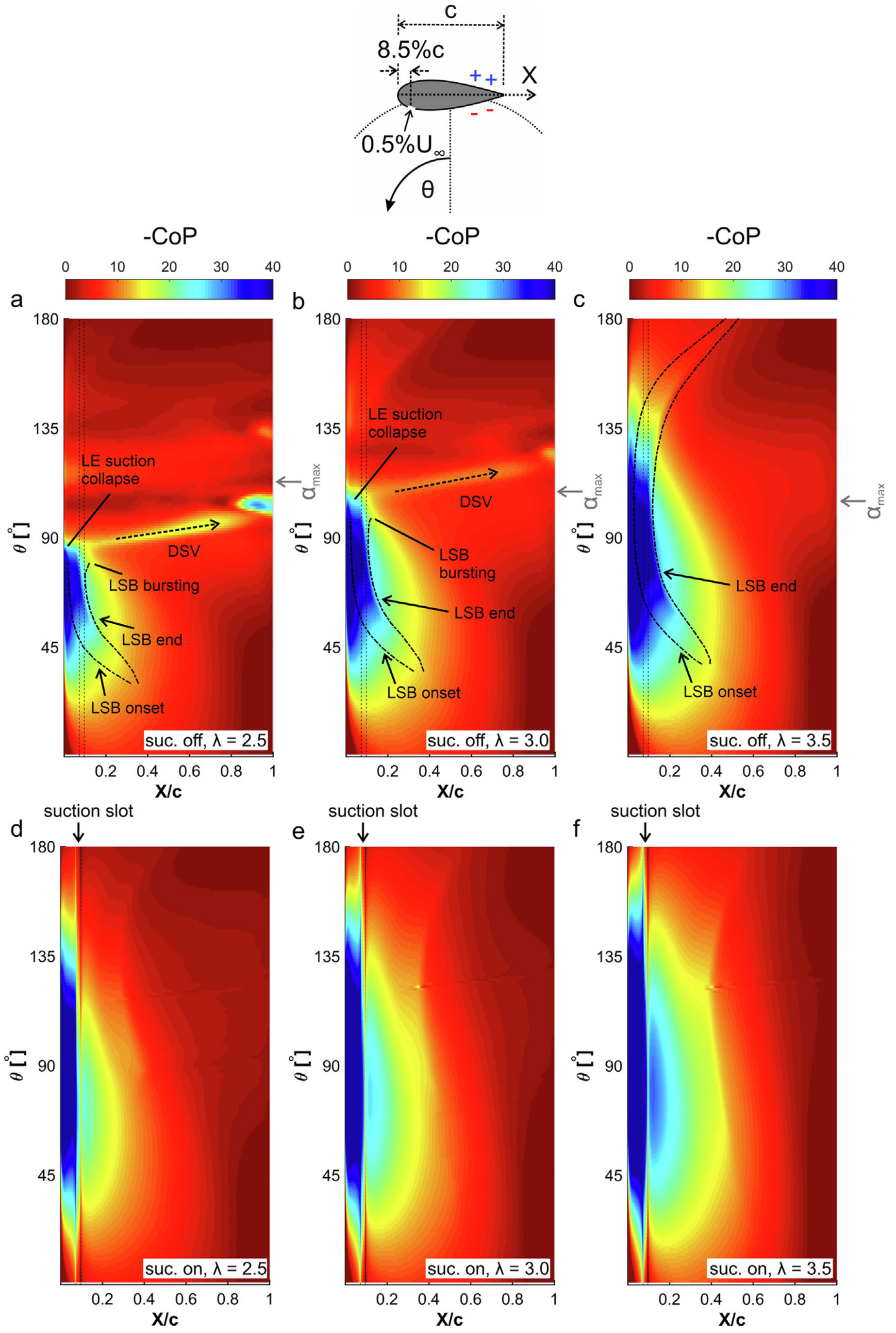

Fig. 9. Spatiotemporal contour plots of surface pressure coefficient along the blade suction side during the turbine half-revolution. LSB: laminar separation bubble; DSV: dynamic stall vortex; LE: leading edge. Note that the X-axis is oriented along the chord and rotating along with the blade. The vertical dashed lines in sub-fig. a-c show the suction location.

suction and negative friction stemming from the LSB towards the trailing-edge, (iii) trailing-edge roll-up vortex (TEV): the TEV, which rolls up from the pressure side towards the suction side at the trailing edge when the DSV detaches from the surface, is rotating the opposite direction of the DSV, thus, is recognized by a positive friction imprint near the trailing edge, and (iv) turbulent trailing-edge (TE) separation: the TE separation is recognized by an incipient negative friction imprint from the trailing edge towards the leading edge. Indications are included in Figs. 8–9 for clarity and further explanations are provided in Refs. [7,19].

Fig. 10 illustrates contour plots of the instantaneous dimensionless tangential velocity ($V_{tan,n}$), defined using Eq. (1) which is based on the fixed coordinate system denoted by X″ and Y″ in the schematic shown on top of Fig. 10, with superimposed streamlines at different azimuthal positions for $\lambda = 2.5$. Note that similar observations, but to a lesser magnitude, are also observed for the other tip speed ratios of 3.0 and 3.5, which for brevity are not shown here. A schematic of the coordinate system and the presented azimuthal positions is shown on top of the figure. The figure is presented to highlight the reverse flow regions along the blade surface with suction off and on.

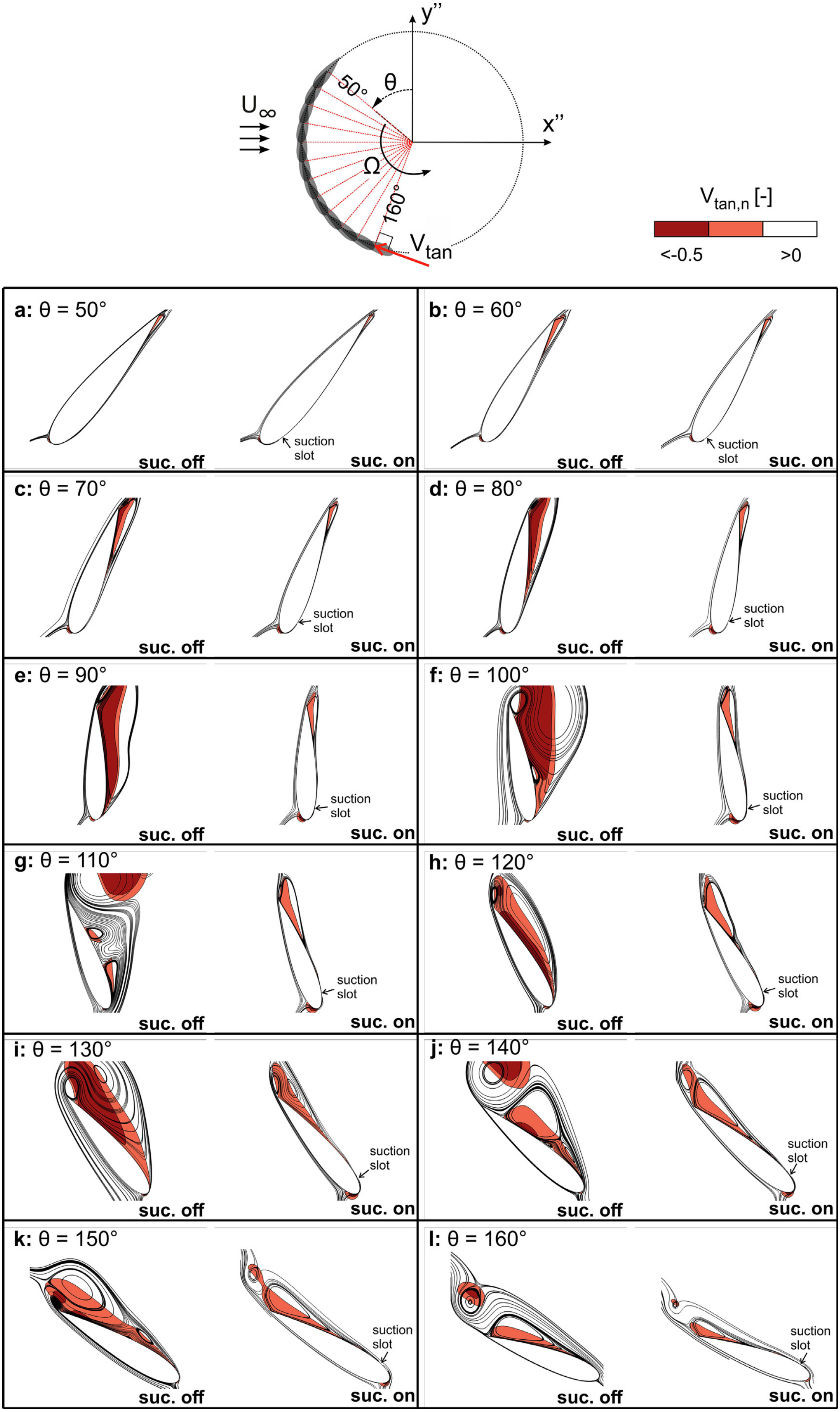

Fig. 10. Contour plots of instantaneous dimensionless tangential velocity (defined using Eq. (1) on the fixed coordinate system denoted by X″ and Y″) with superimposed streamlines. A schematic of the coordinate system and the presented azimuthal positions is shown on top of the figure. ($\lambda = 2.5$).

$$V_{tan,n} = (u\cos(\theta) + v\sin(\theta))/U_\infty \tag{1}$$

Before elaborating on the influence of boundary layer suction, first, several observations for the reference turbine with suction off are discussed based on Figs. 7–10:

- Fig. 8a – c: By decreasing λ from 3.5 to 2.5, the LSB moves towards the leading-edge due to higher variations of α. Note that increasing α is known to shift the LSB upstream along the blade surface [59,74].
- Fig. 9a – c: By decreasing λ from 3.5 to 2.5, the chordwise extent of the LSB decreases due to higher variations of α.
- Fig. 8a – b, 9a – b and 10: At $\lambda = 2.5$ and 3.0, the occurrence of the dynamic stall is observed on the blade where the DSV is formed, propagated downstream and finally shed. For $\lambda = 3.0$, the shedding of the DSV occurs later due to more limited variations of α.
- Fig. 8a – b and 10: At $\lambda = 2.5$ and 3.0, by the shedding of the DSV, TEV is found to roll up near the trailing edge.
- Fig. 8c: At $\lambda = 3.5$, the dynamic stall is avoided on the blade and the LSB persists in existing near the leading edge. Although Fig. 6c shows that α exceeds the α_{SS}, however, during the upstroke (increasing α) the boundary layer is known to be more resistant to separation compared to the static case [25,59,74].

Based on Figs. 7–10, the following observations regarding the influence of boundary layer suction through a slot near the leading edge ($X_S/c = 8.5\%$ and $A_S = 0.5\%$) are made:

- For all cases, the suction slot is positioned along the LSB extent (predicted based on 'suc. off' case).
- At $\lambda = 2.5$ and 3.0, applying boundary layer suction suppresses the dynamic stall and avoids the formation of the DSV. In addition, the TEV is also avoided using suction. At $\lambda = 3.5$ where dynamic stall does not occur, applying boundary layer suction postpones the LSB formation and the trailing-edge separation.
- Applying suction either prevents the LSB formation, e.g. at $\lambda = 2.5$ the LSB is avoided from $\theta \approx 40°$ to $\approx 80°$, or postpones the LSB further downstream along the chord, e.g. at $\lambda = 3.5$ and $\theta = 90°$ the LSB onset is postponed from $\approx 3\%c$ to $29\%c$, where c denotes the blade chord length.
- Applying suction delays the trailing-edge separation, where this is more pronounced for $\lambda = 3.5$ (see Fig. 8f).

Note that the diagonal lines, which appear at $115° < \theta < 130°$ and $X/c > 0.3$ in the skin friction and pressure coefficient contours shown in Figs. 8 and 9 are found to be due to the local interaction of the downstream-travelling trailing-edge separation with a small separation bubble formed at the blade mid-chord.

Figs. 11–13 show the aerodynamic load coefficients, namely lift and drag coefficients C_l and C_d, versus azimuth θ and angle of attack α during the turbine half-revolution at $\lambda = 2.5$, 3.0 and 3.5. It can be seen that by applying boundary layer suction:

- For all cases, negligible differences in aerodynamic loads are found within $0° \leq \theta < 45°$ corresponding to where the LSB is not yet well developed for the 'suc. off' case.
- For all cases, for θ from 45° to $\approx 60°$ where α almost reaches α_{SS}, the drag values decrease while the lift values remain almost unchanged. This is thought to be due to avoiding/postponing the LSB which could lead to maintaining a laminar boundary layer along a larger fraction of the blade surface. This could result in lower skin friction values compared to the turbulent boundary layer downstream of the LSB for the turbine with suction off.

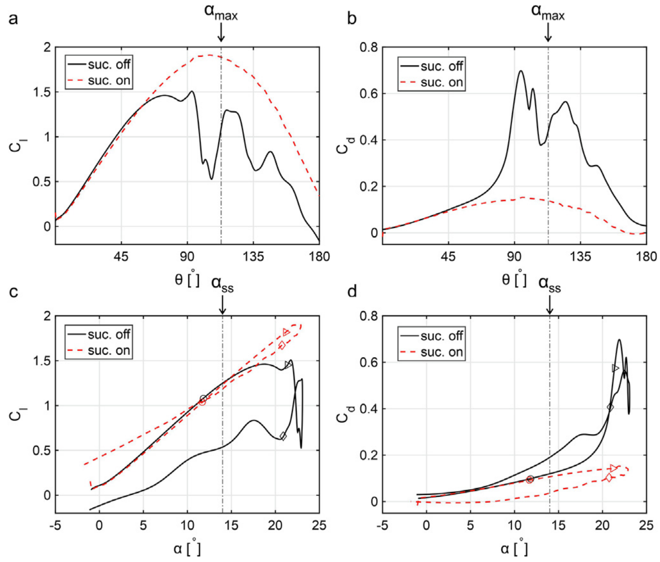

Fig. 11. Aerodynamic load coefficients during the turbine half-revolution at $\lambda = 2.5$ (○: $\theta = 45°$; ▷: $\theta = 90°$; ◊: $\theta = 135°$).

- For all cases, for $\theta > 60°$, corresponding to $\alpha > \alpha_{SS}$, the lift values increase while the drag remains lower than the turbine with suction off. This is due to significantly more limited separation along the blade for the 'suc. on' case.
- For $\lambda = 2.5$ and 3.0, the dynamic stall, which is recognized by a sudden reduction in the lift and an abrupt jump in the drag and consequent load fluctuations, is clearly avoided.
- For all cases, the slope of the $C_l - \alpha$ curve during the upstroke remains almost untouched with respect to the 'suc. off' case. However, this slope is slightly higher than the 'suc. off' case during the downstroke.
- For all cases, $C_{l,max}$ has significantly increased while $C_{d,max}$ has substantially decreased. The change is more noticeable at lower λ where the dynamic stall is more dominant.

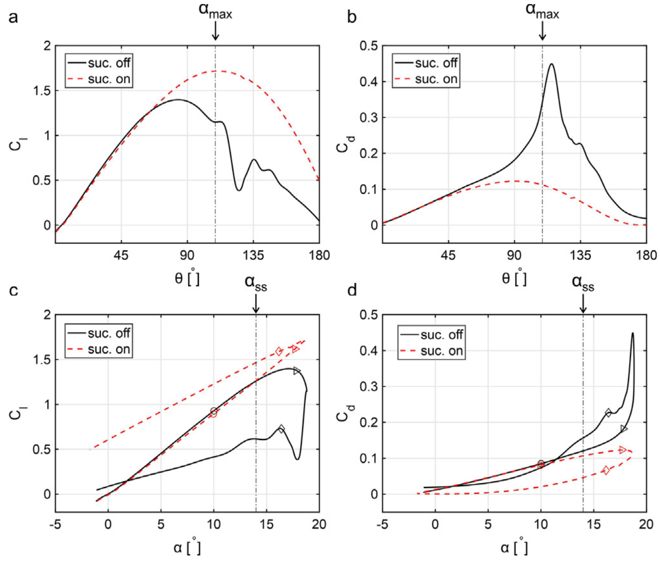

Fig. 12. Aerodynamic load coefficients during the turbine half-revolution at $\lambda = 3.0$ (○: $\theta = 45°$; ▷: $\theta = 90°$; ◊: $\theta = 135°$).

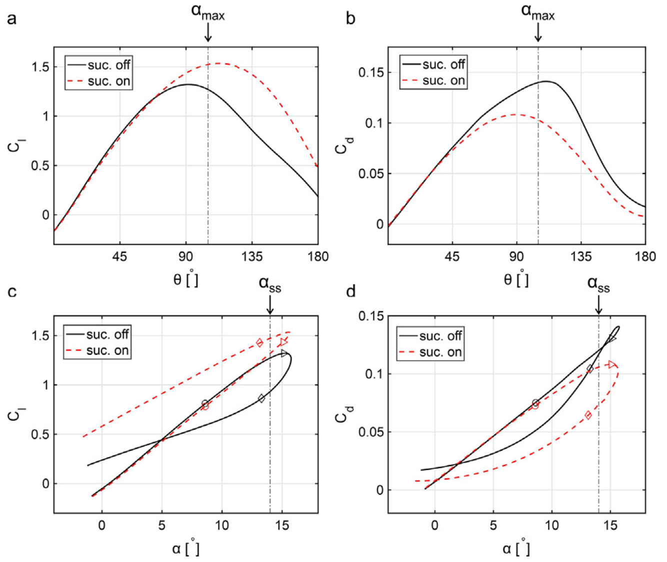

Fig. 13. Aerodynamic load coefficients during the turbine half-revolution at $\lambda = 3.5$ (○: $\theta = 45°$; ▷: $\theta = 90°$; ◊: $\theta = 135°$).

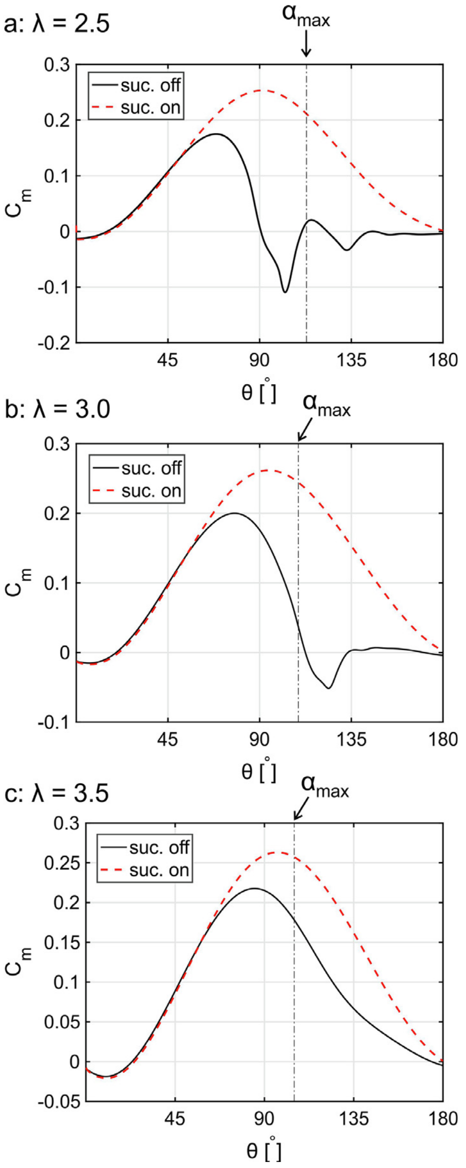

Fig. 14. Turbine instantaneous moment coefficient during the turbine half-revolution.

4.2. Turbine power performance

Table 4 presents the turbine power coefficient for the reference turbine with suction off and on and the overall power gain, in term of ΔC_P, due to the boundary layer suction for the reference case, see Table 1. Fig. 14 shows the turbine instantaneous moment coefficient, C_m, during the turbine half-revolution for different tip speed ratios.

It can be seen that by applying the suction, at $\lambda = 2.5$ where the turbine experiences a deep dynamic stall, the turbine C_m is unchanged for θ up to $\approx 53°$. For $\theta > 53°$, the turbine C_m is substantially improved due to the suction and consequently, the turbine C_P is significantly enhanced by 246.6%. The peak in C_m is also shifted from $\theta = 68°-91°$ due to the suction. This shift is because of the delayed stall on the blade. The sudden reduction in C_m (at $68° < \theta < 103°$) and the subsequent fluctuations (at $103° < \theta < 145°$), which occur for the turbine with suction off due to the dynamic stall on the blade, are visibly prevented by suction. At $\lambda = 3.0$, where the turbine goes into a comparatively light dynamic stall, and at $\lambda = 3.5$, where the dynamic stall is avoided, the trend of the change in C_m due to the suction is similar to $\lambda = 2.5$, however, the turbine power gain is comparatively less. The turbine C_P values at $\lambda = 3.0$ and $\lambda = 3.5$ are increased by 83.2% and 24.4%, respectively. The average power gain over all the λ values is 118.1%.

4.3. Impact of suction amplitude and location

In this section, the influence of suction amplitude and suction slot location is analyzed for the reference turbine at reference operating conditions given in Table 1. Table 5 presents the details of the studied cases. For the suction amplitude, a wide range of A_S from 0.5% to 10% is studied. Regarding the suction location, four different locations near the leading edge of the turbine blade are analyzed. The center locations of the suction slots are $X_S/c = 8.5\%$, 13.5%, 18.5% and 28.5%. The start and end locations of the suction slots are given in Table 5. As the impact of suction slot width is known to be minimal [75,76], therefore, in the present study the width of the suction slot is kept constant, i.e. $W/c = 2.5\%$.

First, the suction slot is fixed at $X_S/c = 8.5\%$ and the suction amplitude is varied. Table 6 presents the turbine power gain as a function of suction amplitude for $A_S = 0.5-10\%$. Fig. 15 presents the spatiotemporal contour plots of skin friction coefficient, C_f, along the blade suction side (inner side) during the turbine half-revolution for $A_S = 0.5\%$ and 10%. Fig. 16 shows the turbine instantaneous moment coefficient during the turbine half-revolution for $A_S = 0.5\%$ and 10%. Within the studied range, the impact of suction amplitude is found to be insignificant where the turbine power gain, the turbine instantaneous moment and the critical boundary layer events along the blade suction side are minimally influenced by suction amplitude. At $\lambda = 2.5$, by

Table 4
Turbine power gain due to boundary layer suction.

λ	C_P		ΔC_P [%]
	suc. Off	suc. On	
2.5	0.045	0.156	246.6
3.0	0.137	0.251	83.2
3.5	0.254	0.316	24.4
Average over all λ			118.1

Table 5
Details of the studied parameters for the reference turbine.

Parameter			Value				
Suction slot	Location	Case	suc 1	suc 2	suc 3	suc 4	
		Start, $X_{S,1}/c$ [%]	7.33	12.33	17.33	27.33	
		Center, X_S/c[%]	8.50	13.50	18.50	28.50	
		End, $X_{S,2}/c$ [%]	9.83	14.83	19.83	29.83	
	Width, W/c [%]		2.5				
	Amplitude	Case	amp 1	amp 2	amp 3	amp 4	amp 5
		A_S [%]	0.5	1.0	2.5	5.0	10.0

Table 6
Turbine power gain as a function of suction amplitude. ($X_S/c = 8.5\%$).

λ	ΔC_P [%]				
	$A_S = 0.5\%$	$A_S = 1\%$	$A_S = 2.5\%$	$A_S = 5\%$	$A_S = 10\%$
2.5	246	246	248	251	259
3.0	83	83	84	84	85
3.5	24	24	24	24	25
Average over all λ	118	118	119	120	123

increasing A_S from 0.5% to 10% (i.e. a factor of 20 times higher), the power gain marginally increases from 246% to 259% (i.e. a factor of 1.05 times higher). The power gain with increasing suction amplitude is even less pronounced at higher λ of 3.0 and 3.5. Similar observations are found (not shown here for brevity) when the suction slot is fixed at the other suction locations, i.e. $X_S/c = 13.5\%$, 18.5% and 28.5%, and the suction amplitude is varied within $A_S = 0.5-10\%$.

Second, the suction amplification is fixed at $A_S = 0.5\%$ and the suction slot location is varied. Table 7 presents the turbine power gain as a function of suction location for $X_S/c = 8.5\%$, 13.5%, 18.5% and 28.5%. Fig. 17 presents the spatiotemporal contour plots of skin friction coefficient, C_f, along the blade suction side (inner side) during the turbine half-revolution for different suction locations. Fig. 18 shows the turbine instantaneous moment coefficient during the turbine half-revolution for different suction locations. Within the studied range, the impact of the suction location is found to be significant, where the turbine power gain, the instantaneous moment and the critical boundary layer events along the blade suction side are substantially influenced by suction location. At $\lambda = 2.5$, by shifting the suction slot downstream towards the trailing edge from $X_S/c = 8.5\%-13.5\%$, the power gain, in terms of ΔC_P, reduces from 246% to 208%. The respective C_m values also noticeably decrease for $\theta > 80°$. The skin friction plots reveal that by this shift, the suction location is moved slightly downstream of the location of the LSB for 'suc. off' case. Nevertheless, the dynamic stall is still avoided due to the suction. Further downstream shifts of the suction slot to 18.5% and 28.5% more substantially diminish the turbine power gain to 119% and 81%, respectively. Fig. 18a also shows that the C_m values monotonically decrease due to the downstream shift. For the two most downstream suction locations, i.e. $X_S/c = 18.5\%$ and 28.5%, the suction slot is already too downstream of the LSB, which therefore cannot prevent its shedding and consequently the dynamic stall, recognized by the formation of the DSV, persists on the blade despite the suction.

The skin friction contours shown in Fig. 17 reveal that when the suction slot is located at 8.5%c, it is positioned right along the LSB for the turbine with suction off, therefore, applying suction can noticeably suppress the LSB and avoid the dynamic stall. However, when the suction slot is shifted further towards the trailing edge, its position moves to downstream of the LSB, thus applying suction will have much more limited influence on the critical flow features. These observations imply that in order to most effectively suppress the separation using boundary layer suction, the suction slot needs to be positioned along the LSB.

Overall, similar observations for the higher λ of 3.0 and 3.5 are made although here ΔC_P is much less sensitive to the suction location. The less sensitivity could be attributed to the larger chordwise extent of the LSB for the higher λ, see Fig. 9b and c. In addition, for $\lambda = 3.5$, the ΔC_P for suction location at 13.5% is marginally higher than 8.5%, unlike the lower λ values. This is because for higher λ, where the variations of α are more limited, the LSB is slightly shifted downstream for the turbine with suction off (see Section 4.1). Therefore, the optimum suction location is also a bit further downstream than the lower λ. Similar observations are found (not shown here for brevity) when the suction amplitude is fixed at the other amplitudes, i.e. $A_S = 1-10\%$, and the suction location is varied for $X_S/c = 8.5\%$, 13.5%, 18.5% and 28.5%.

5. Dependency of optimal suction characteristics on operational parameters

In this section, the dependency of the turbine power gain due to the boundary layer suction through a slot near the leading edge on the operational parameters is investigated for the reference turbine. For every single operational parameter and each individual value, 20 different cases (consisting of 4 suction locations and 5 suction amplitudes) are investigated to find the individual local optimal suction characteristics at the given condition.

In general, the dependency of the optimal suction characteristics on operational parameters is important because for a turbine in real conditions, the operational parameters inevitably change. Therefore, if the suction system is to work optimally at a range of operational parameters, it might need to be designed with multiple locations and adaptable amplitude so that based on the real-time conditions the respective optimal suction is operated. Needless to say, such a system would need a set of sensors and a feedback control loop.

The suction characteristics are as given in Table 5. The studied parameters are (i) tip speed ratio, (ii) Reynolds number and (iii) turbulence intensity. Table 8 presents the details of the studied parameters.

i. *Tip speed ratio*: Three different tip speed ratios of 2.5, 3.0 and 3.5 are investigated. Note that although the results in Section 4 are presented for different λ, however, the provided discussions did not aim to elucidate the impact of λ on optimal suction characteristics, which is the focus of this section. The range covers low tip speed ratios, where the turbine blades experience a deep dynamic stall, and moderate tip speed ratios where the variations of the angle of attack during the revolution are more limited and light dynamic stall might occur.
ii. *Reynolds number*: The chord-based Reynolds number varies from $0.51 \times 10^5-2.78 \times 10^5$, where the range is corresponding to the operational regime for small-scale VAWTs [2].

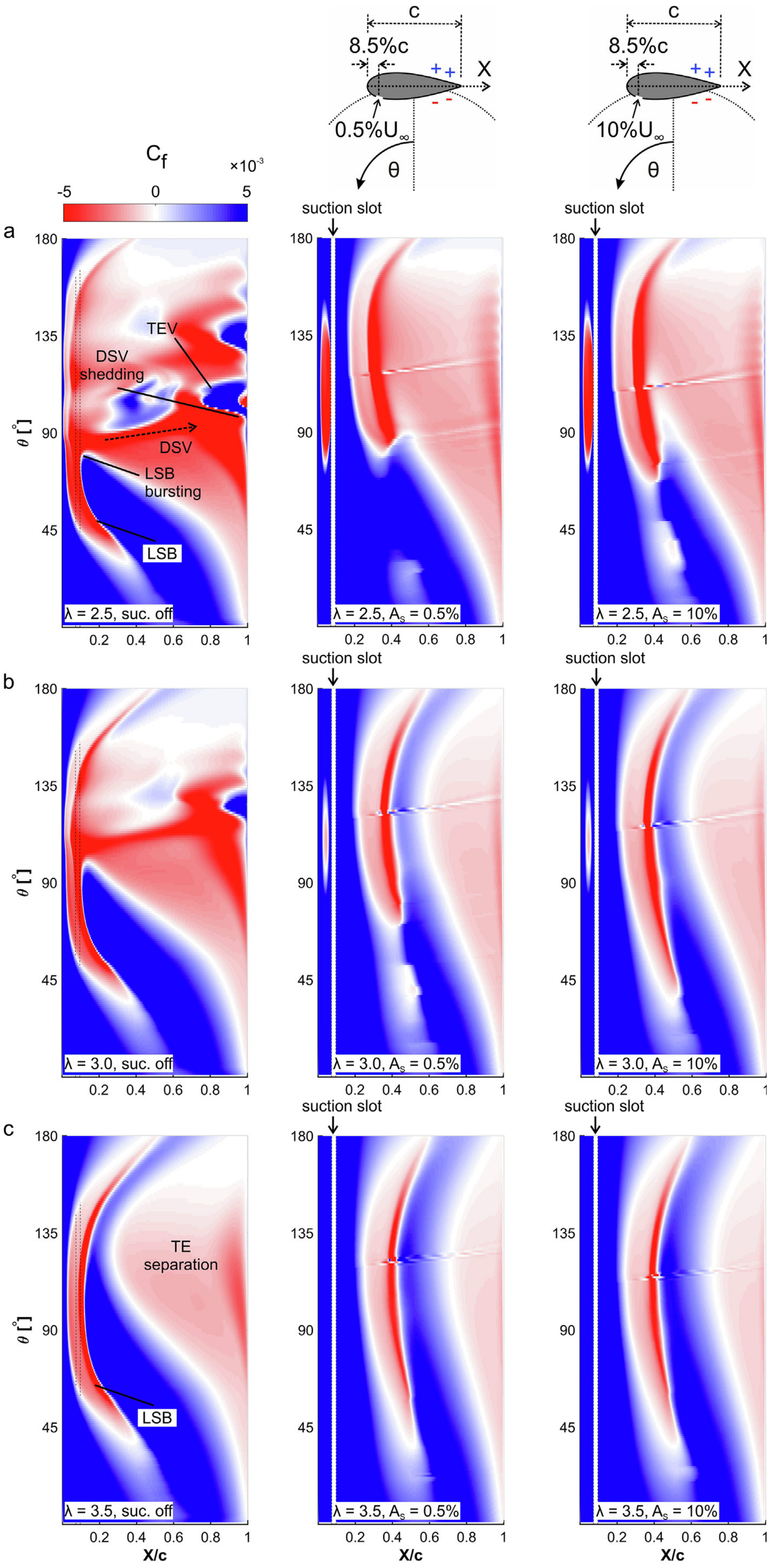

Fig. 15. Spatiotemporal contour plots of skin friction coefficient along the blade suction side during the turbine half-revolution. LSB: laminar separation bubble; DSV: dynamic stall vortex; TE: trailing edge; TEV: trailing-edge roll-up vortex. ($X_S/c = 8.5\%$).

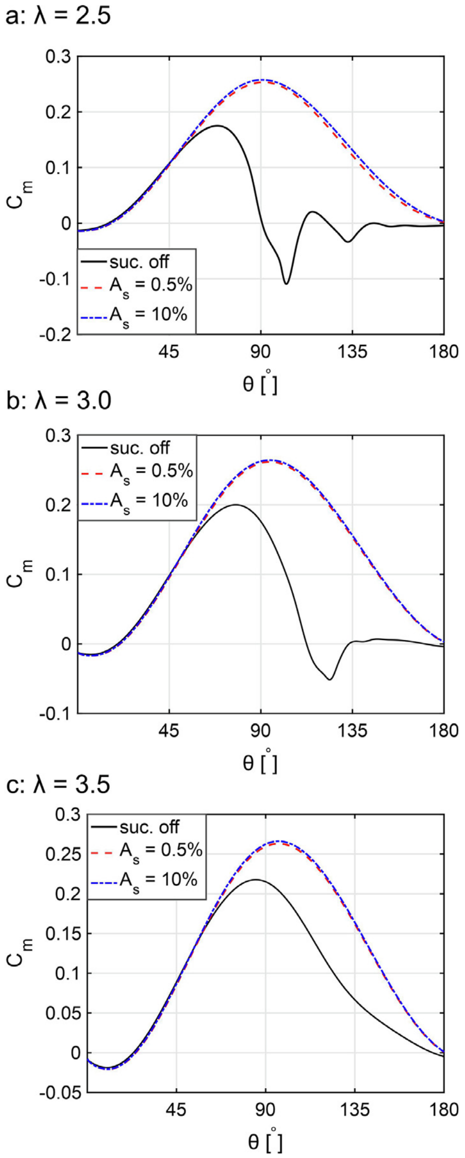

Fig. 16. Turbine instantaneous moment coefficient during the turbine half-revolution. ($X_S/c = 8.5\%$).

iii. *Turbulence intensity*: Three values of approach-flow total TI are studied, i.e. 1%, 5% and 25%, to analyze the sensitivity of the findings to TI in a range from low TI levels relevant for wind-tunnel experiments to moderately high values corresponding to operational conditions in high turbulence areas.

5.1. *Impact of tip speed ratio*

Table 9 presents the optimal suction location as a function of tip speed ratio for different suction amplitudes for the reference turbine at reference operating conditions, i.e. TI = 5%, $Re_c \approx 10^5$. The table is prepared using 60 URANS simulations, i.e. the optimal values at each λ are based on 20 URANS simulations. Fig. 19 shows the contour maps of the turbine power gain, in terms of ΔC_P, in 'suction amplitude − suction location' space. The maps help to identify the optimal suction characteristics as a function of tip speed ratio. Within the studied range, the following observations are made:

- In general, the power gain due to suction remarkably decreases with increasing λ. For example, with a suction amplitude of 0.5%, the power gain at λ of 2.5, 3.0 and 3.5 is 246%, 83% and 25%, respectively. The more prominent influence of suction at lower λ is because at lower λ the turbine aerodynamic performance is highly dominated by flow separation, thus, its suppression will have a strong impact on the overall power performance. Note that the changes in the absolute values of C_P are: (i) at λ = 2.5, the C_P value increases from 0.045 to 0.156; (ii) at λ = 3.0, the C_P value increases from 0.137 to 0.251; and (iii) at λ = 3.5, the C_P value increases from 0.254 to 0.316.
- The optimal suction location slightly shifts downstream as λ increases. For λ = 2.5 and 3.0, the optimal suction location is at 8.5%*c* while this shifts to 13.5%*c* for λ = 3.5, where *c* is the blade chord length. Note that at λ = 3.5, the power gain due to suction at 13.5%*c* is marginally higher than 8.5%*c*, i.e. only 1%. Nevertheless, the shift is due to the modest downstream shift of the LSB at higher λ, as discussed in Section 4.1.
- The optimal range of suction location, which can be inferred from the red regions in contour plots in Fig. 19, becomes wider as λ increases. This is because of the increase in the chordwise extent of the LSB for higher λ, as discussed in Section 4.1.
- The optimal suction location is independent of the suction amplitude.

In short, applying suction at $X_S/c = 8.5\%$ is found to be effective for the majority of studied tip speed ratios. At the highest λ of 3.5, despite the slight downstream shift of the LSB, a suction slot with 8.5%*c* is still located along the LSB and provides results comparable to the optimal location of 13.5%*c*. Therefore, it can be concluded that for the reference turbine at the reference operating condition, i.e. TI = 5% and $Re_c \approx 10^5$, a single leading-edge suction slot location can be selected to effectively suppress the flow separation at different tip speed ratios and to enhance the VAWT power performance. The sensitivity of the optimal suction location to tip speed ratio can be considered insignificant.

In this regard, for typical constant-speed VAWTs, whose tip speed ratio inevitably changes with varying freestream velocity, the location of the suction slot can be configured near the blade leading edge to align the LSB location in order to effectively suppress the flow separation at low tip speed ratios.

Table 7
Turbine power gain as a function of suction location. ($A_S = 0.5\%$).

λ	ΔC_P [%]			
	$X_S/c = 8.5\%$	$X_S/c = 13.5\%$	$X_S/c = 18.5\%$	$X_S/c = 28.5\%$
2.5	246	208	119	81
3.0	83	79	65	44
3.5	24	25	22	13
Average over all λ	118	104	69	46

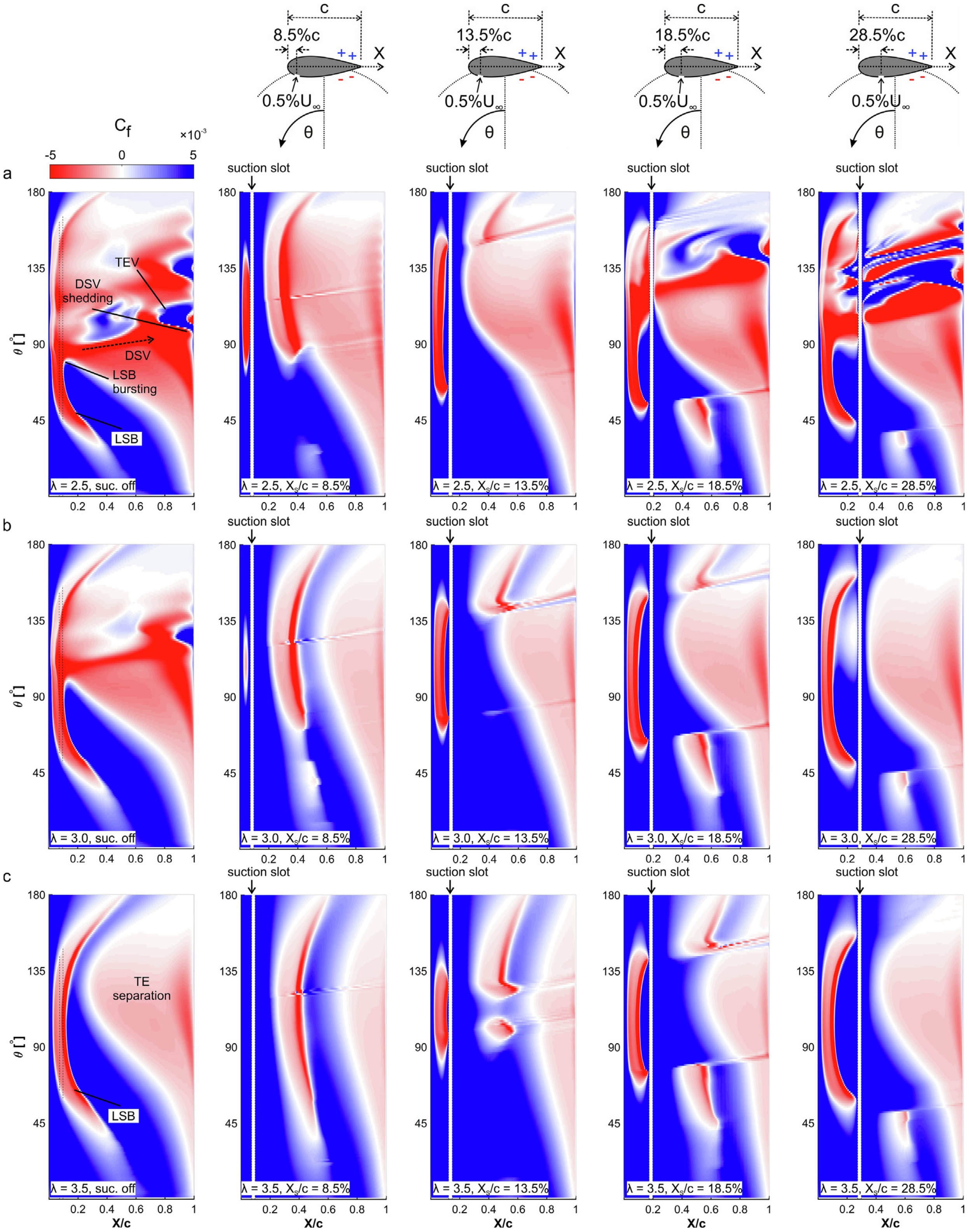

Fig. 17. Spatiotemporal contour plots of skin friction coefficient along the blade suction side during the turbine half-revolution. LSB: laminar separation bubble; DSV: dynamic stall vortex; TE: trailing edge; TEV: trailing-edge roll-up vortex. (A_S = 0.5%).

5.2. Impact of turbulence intensity

Table 10 presents the optimal suction location as a function of turbulence intensity for different suction amplitudes for $Re_c \approx 10^5$. The table is prepared using 60 URANS simulations, i.e. the optimal values at each TI are based on 20 URANS simulations. Fig. 20 shows the contour maps of the turbine power gain, in terms of ΔC_P, in 'suction amplitude – suction location' space. The maps help to identify the optimal suction characteristics as a function of TI. Within the studied range, the following observations are made:

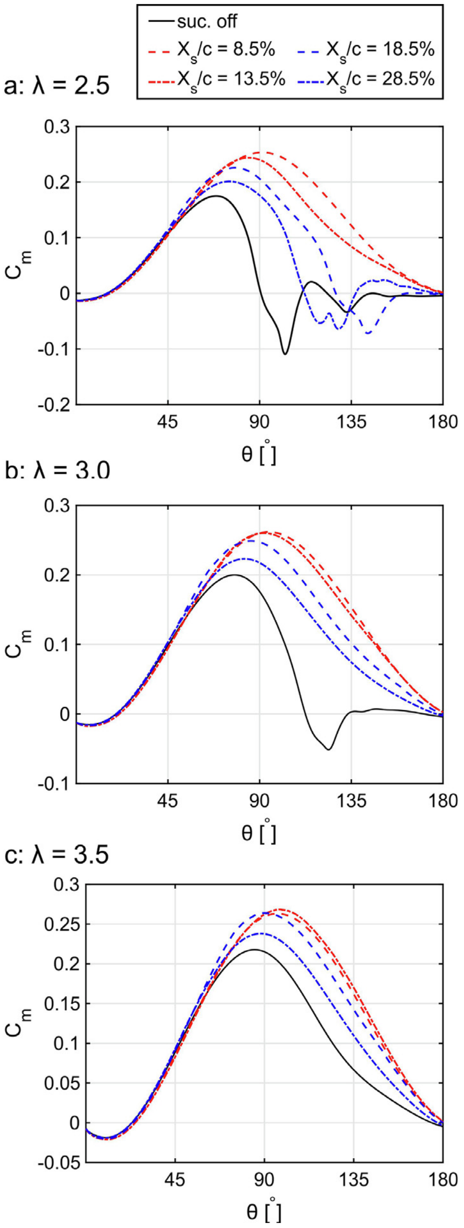

Fig. 18. Turbine instantaneous moment coefficient during the turbine half-revolution. (A_S = 0.5%).

Table 8
Details of the operational conditions of the test cases for the reference turbine.

U_∞ [m/s]	Ω [rad/s]	λ	Re_c [× 10^5]		TI [%]	TI_i [%]
			Re-class	Value		
4.65	23.25	2.5	0.5 × 10^5	0.51	1.0	0.95
4.65	27.90	3.0		0.60	5.0	3.96
4.65	32.55	3.5		0.69	25.0	12.3
9.3	46.50	2.5	1.0 × 10^5	1.03		
9.3	55.80	3.0		1.21		
9.3	65.10	3.5		1.39		
18.6	93.00	2.5	2.0 × 10^5	2.06		
18.6	111.60	3.0		2.42		
18.6	130.20	3.5		2.78		

Table 9
Optimal suction location, X_S/c [%], and the respective turbine power gain as a function of tip speed ratio. The optimal values at each λ, presented in the table, are based on 20 URANS simulations. (TI = 5%, $Re_c \approx 10^5$).

	λ		
Parameter	**2.5**	**3.0**	**3.5**
Optimal X_S/c [%]	**8.5**	**8.5**	**13.5**
ΔC_P [%] at A_S = 0.5%	246	83	25
ΔC_P [%] at A_S = 10.0%	259	85	26

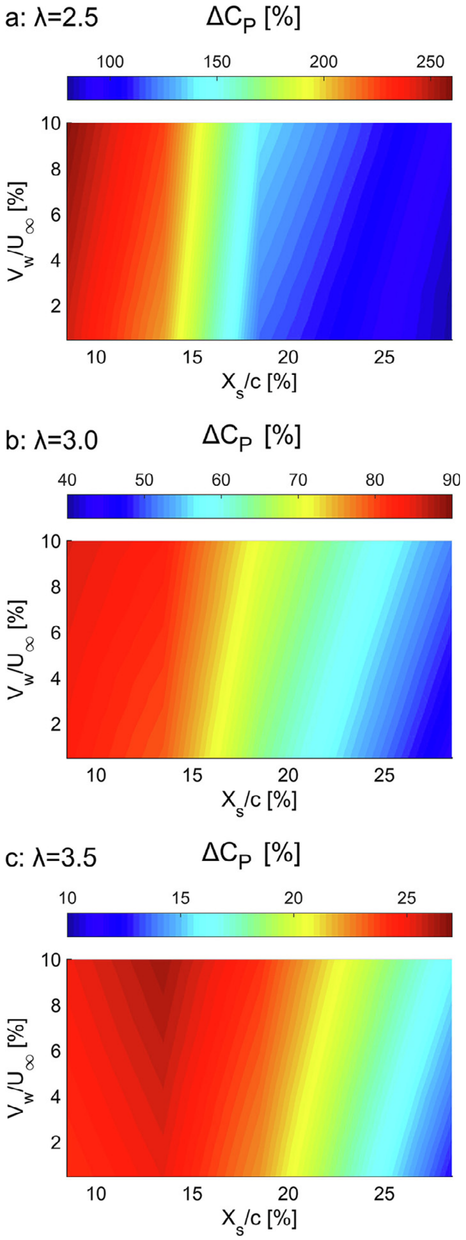

Fig. 19. Contour maps of turbine power gain in suction amplitude – suction location space. Each plot is based on 20 CFD simulations. (TI = 5%, $Re_c \approx 10^5$).

- In general, the power gain due to suction remarkably decreases with increasing TI at all λ. For example, at λ = 3.0 with suction amplitude of 0.5%, the power gain at TI of 1%, 5% and 25% is 249%, 83% and 32%, respectively. The more prominent influence of suction at lower TI is because at lower TI, the boundary layer

Table 10
Optimal suction location, X_S/c [%], and the respective turbine power gain as a function of TI for different tip speed ratios. The optimal values at each TI, presented in the table, are based on 20 URANS simulations. ($Re_c \approx 10^5$).

		λ		
TI	Parameter	**2.5**	**3.0**	**3.5**
1%	Optimal X_S/c [%]	**8.5**	**8.5**	**13.5**
	ΔC_P [%] at $A_S = 0.5\%$	1133	249	54
	ΔC_P [%] at $A_S = 10.0\%$	1134	253	54
5%	Optimal X_S/c [%]	**8.5**	**8.5**	**13.5**
	ΔC_P [%] at $A_S = 0.5\%$	246	83	25
	ΔC_P [%] at $A_S = 10.0\%$	259	85	26
25%	Optimal X_S/c [%]	**8.5**	**8.5**	**13.5**
	ΔC_P [%] at $A_S = 0.5\%$	94	32	12
	ΔC_P [%] at $A_S = 10.0\%$	99	34	13

on the blade is less resistant to flow separation, thus, the turbine aerodynamic performance is comparatively more dominated by separation and its suppression by suction will result in a stronger enhancement of the turbine power performance.

- Within the studied cases ($1\% \leq TI \leq 25\%$), the optimal suction location is minimally affected by the TI. Note that by increasing TI, the LSB moves slightly upstream and its chordwise extent decreases. The upstream shift in the position of the LSB for higher TI might suggest that at high TI and low λ, applying suction closer to the leading edge, $X_S/c < 8.5\%$, could be even more promising. Nevertheless, the suction location of 8.5%*c* is effective for the majority of conditions while providing comparable power gain to the optimal value for the other cases where 13.5%*c* is optimal.
- The optimal range of suction location, which can be inferred from the red regions in contour plots in Fig. 20, becomes wider as TI increases. At λ = 2.5, for TI = 1%, 5% and 25% the turbine with suction off operates in dynamic stall and applying suction at 8.5%*c* and 13.5%*c* can suppress that. Suction at 18.5%*c* is only effective to suppress the dynamic stall for TI = 25% and suction at 28.5%*c* is ineffective in dynamic stall suppression for all TI. At λ = 3.0, for TI = 1% and 5% the turbine with suction off operates in dynamic stall while due to the high turbulence level of the incoming flow, dynamic stall is already avoided at TI = 25%. Applying suction at 8.5%*c*, 13.5%*c* and 18.5%*c* can suppress the dynamic stall at TI = 1% and 5%. Suction at 28.5%*c* is only effective to suppress the dynamic stall for TI = 5% and not at TI = 1%. At λ = 3.5, only for TI = 1% the turbine with suction off

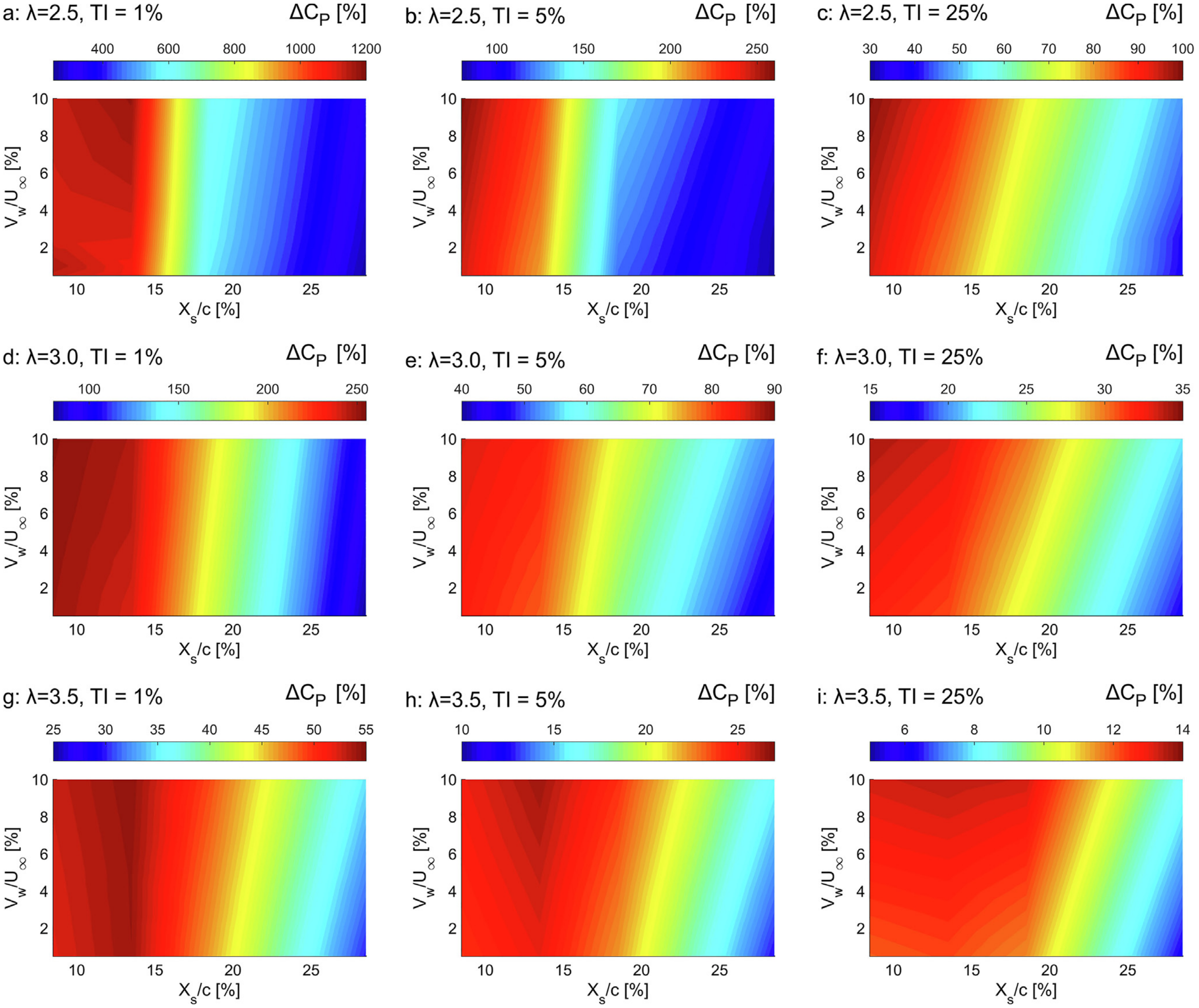

Fig. 20. Contour maps of turbine power gain in suction amplitude – suction location space. Each plot is based on 20 CFD simulations. ($Re_c \approx 10^5$).

Table 11
Optimal suction location, X_S/c [%], and the respective turbine power gain as a function of Re_c for different tip speed ratios. The optimal values at each Re_c presented in the table is based on 20 URANS simulations. (TI = 5%).

		λ		
Re_c	Parameter	**2.5**	**3.0**	**3.5**
$\approx 0.5 \times 10^5$	Optimal X_S/c [%]	**13.5**	**13.5**	**13.5**
	ΔC_P [%] at $A_S = 0.5\%$	595	193	62
	ΔC_P [%] at $A_S = 10.0\%$	628	194	63
$\approx 1 \times 10^5$	Optimal X_S/c [%]	**8.5**	**8.5**	**13.5**
	ΔC_P [%] at $A_S = 0.5\%$	246	83	25
	ΔC_P [%] at $A_S = 10.0\%$	259	85	26
$\approx 2 \times 10^5$	Optimal X_S/c [%]	**8.5**	**8.5**	**8.5**
	ΔC_P [%] at $A_S = 0.5\%$	136	36	13
	ΔC_P [%] at $A_S = 10.0\%$	143	37	13

experiences dynamic stall and that is avoided by applying suction at 8.5%*c*, 13.5%*c* and 18.5%*c* and 28.5%*c*.

- The optimal suction location is independent of the suction amplitude.

In short, the optimal suction location is weakly sensitive to TI. Therefore, an optimal suction location set for a turbine based on numerical/experimental analyses at lower TI, can also work optimally at higher TI in operational conditions.

5.3. *Impact of Reynolds number*

Table 11 presents the optimal suction location as a function of chord-based Reynolds number for different suction amplitudes for TI = 5%. Note that, as detailed in Table 8, to modify Re_c, the values of both the freestream velocity and the turbine rotational velocity are modified. The table is prepared using 60 URANS simulations, i.e. the optimal values at each Re_c are based on 20 URANS simulations. Fig. 21 shows the contour maps of the turbine power gain, in terms of ΔC_P, in 'suction amplitude − suction location' space. The maps help to identify the optimal suction characteristics as a function of Re. Within the studied range, the following observations are made:

- In general, the power gain due to suction considerably decreases for higher Re_c at all λ. For example, at λ = 3.0 with suction amplitude of 0.5%, the power gain at Re_c of $\approx 0.5 \times 10^5$, $\approx 1.0 \times 10^5$ and $\approx 2.0 \times 10^5$ is 193%, 83% and 36%, respectively. The more prominent impact of suction at lower Re_c is because at lower Re_c the boundary layer on the blade is more prone to flow

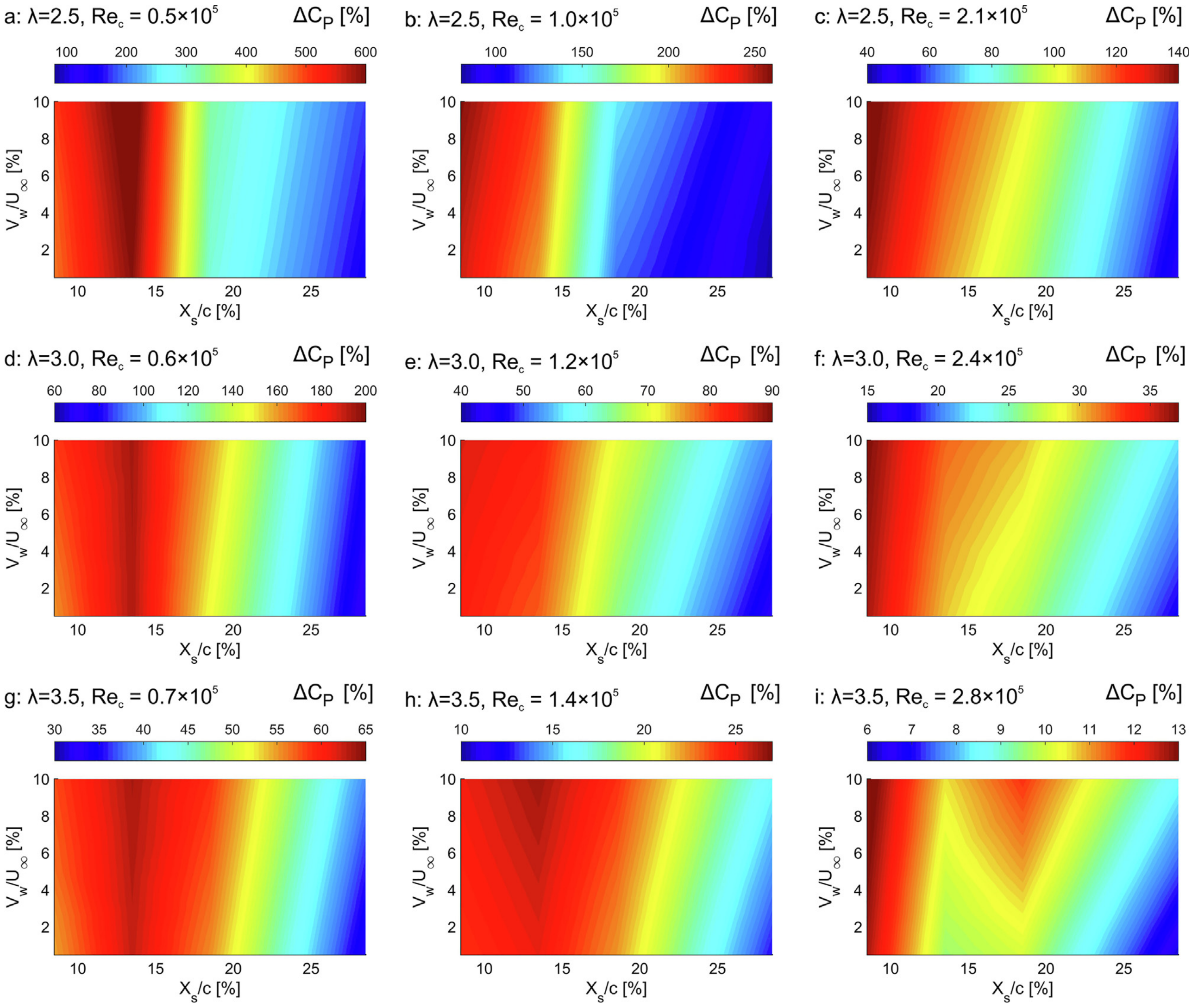

Fig. 21. Contour maps of turbine power gain in suction amplitude − suction location space. Each plot is based on 20 CFD simulations. (TI = 5%).

Table 12
Features of a potential pumping system for a single turbine blade with suction settings given in Table 1.

- Parameter	*- Value*	*- Unit*
Width, W	0.0015	m
Suction velocity, V_W	0.0465	m/s
Volume flow rate per blade with unit span	4.185	l/min
Power consumption of an off-the-shelf vacuum pump (flow rate 5 l/min, *vacuum deeper than* 80 kPa, *voltage 12 V,* e.g. Ref. [77])	4–6	W

Table 13
Estimation of the net power gain due to suction.

λ	C_P		ΔC_P [%]	P [W]				Net power gain [%]
	suc. Off	suc. On		suc. Off	suc. On	Pump input power	Net power gain	
2.5	0.045	0.156	246.6	22.2	76.9	6	70.9	219.6
3.0	0.137	0.251	83.2	67.5	123.7	6	117.7	74.3
3.5	0.254	0.316	24.4	125.1	155.7	6	149.7	19.6
Average over all λ			118.1					104.5

separation, therefore, the turbine aerodynamic performance is comparatively more influenced by separation and its suppression using suction will more significantly enhance the turbine power performance. In this regard, the impact of increasing Re_c is similar to that of increasing TI.

- The optimal suction location is found to move upstream by increasing Re_c from $\approx 0.5 \times 10^5$ to $\approx 1.0 \times 10^5$. This is because by increasing Re_c the chordwise extent of the LSB reduces while the LSB onset location remains almost unaffected. For the same reason, the optimal suction location could have potentially moved further upstream by increasing Re_c to 2.0×10^5, however, $X_S/c = 8.5\%$ is the most upstream location investigated in the present study.
- The optimal suction location is independent of the suction amplitude.

In total, the sensitivity of the optimal suction location to Re_c necessitates that the design of the suction location is set with special attention to the target Re_c.

6. Discussion

Including a suction system on the blades of a wind turbine might impose several practical concerns regarding the structural strength of the blade surface near the suction location, the space needed for installation of the pumping system and the connecting tubes, the location to exhaust the pumped air and the input power for the pumping system.

In order to estimate the required input power for the suction system, a potential pumping system is considered (see Table 12). Note that the pressure losses in the tubing are not considered. For the reference operating condition, see Table 1, an estimation of the new power gain due to the use of the suction system is presented in Table 13. The turbine net power gain due to the suction at $\lambda = 2.5$, 3.0 and $\lambda = 3.5$ is 219.6%, 74.3% and 19.6%, respectively. Due to the low volume flow rate needed for the vacuum pump, the turbine net power gain by the suction is still highly significant and, thus, well justifies its employment.

In the present study, a constant suction amplitude is applied during the whole turbine revolution assuming that the pumping system provides a fixed flow rate regardless of the static pressure along the suction slot. In practice, if the flow rate of the pumping system is a function of the surface pressure along the suction slot, then the suction amplitude might vary during the turbine revolution. However, as shown in Section 4.3, the impact of suction amplitude on the turbine power gain due to suction is negligible. Note that the sucked air can be exhausted via the blade/shaft tips on the top and bottom, which will negligibly influence the turbine structural and aerodynamic performance.

7. Conclusions

Applying suction through a slot near the blade leading edge, along the chordwise extent of the laminar separation bubble (LSB) and upstream of its bursting location, can effectively (i) prevent the LSB bursting; (ii) eliminate the LSB formation or postpone it to downstream of the suction slot; (iii) avoid the formation of the dynamic stall vortex (DSV) and trailing-edge roll-up vortex (TEV) and suppress the dynamic stall phenomena; and (iv) delay the incipient trailing-edge separation.

As a result, the blade lift force and the $C_{l,max}$ significantly increase, the drag force and the $C_{d,max}$ noticeably decrease, the stall angle is postponed, the aerodynamic load fluctuations are suppressed, and the slope of the $C_l - \alpha$ curve during the downstroke increases. Consequently, the instantaneous moment remarkably grows and the turbine power coefficient is very much enhanced.

Applying suction with an amplitude of $A_S = 0.5\%$ for the reference turbine, near the blade leading edge at $X_S/c = 8.5\%$, operating at the reference conditions, $Re_c \approx 10^5$ and TI = 5%, results in a power gain of $\Delta C_P = 247\%$, 83% and 24% at different tip speed ratios of $\lambda = 2.5$, 3.0 and 3.5, respectively. The average power gain over all λ is 118%.

The study of the impact of suction characteristics, namely suction amplitude and location, on the blade aerodynamics and the turbine power performance shows that:

- The impact of suction amplitude on the turbine power gain due to the suction, the turbine instantaneous moment coefficient and the skin friction coefficient along the blade suction side is insignificant within the range studies, where the minimum value of suction amplitude, i.e. 0.5%, is enough to suppress the flow separation.
- The location of the suction slot has a significant influence on the obtained turbine power gain using suction. Such a location needs to be along the chordwise extent of the LSB, optimally towards the downstream end of the LSB. If the slot is positioned further upstream, it still can suppress the separation but the turbine power gain is not optimal. On the other hand, if the slot is positioned too downstream, not overlapping the LSB, the dynamic stall will not be suppressed and the suction will not work effectively.

Regarding the dependency of optimal suction characteristics on the operational parameters (namely tip speed ratio, chord-based Reynolds number and turbulence intensity), the LSB moves slightly upstream and shrinks in chordwise extent for lower λ, higher TI and higher Re_c. The analysis shows that the optimal suction location is insignificantly influenced by TI and minimally influenced by λ while more sensitive to Re_c. Therefore, the suction location needs to be set with special attention to the target Re-regime. When the operational range of λ, TI and Re_c are known, the optimal suction location is best to be set based on the most separation-dominant regime, i.e. lower λ, TI and Re_c, as this is the regime where suction will most effectively enhance the turbine power performance. Of course, in the ideal case, multi-slot suction system needs to be developed so that based on the operating conditions, the optimal suction location is actuated.

Acknowledgement

The authors would like to acknowledge support from the European Commission's Framework Program Horizon 2020, through the Marie Curie Innovative Training Network (ITN) AEOLUS4FUTURE - Efficient harvesting of the wind energy (H2020-MSCA-ITN-2014: Grant agreement no. 643167) and the TU1304 COST ACTION “WINERCOST”. The authors gratefully acknowledge the partnership with ANSYS CFD. This work was sponsored by NWO Exacte Wetenschappen (Physical Sciences) for the use of supercomputer facilities, with financial support from the Nederlandse Organisatie voor Wetenschappelijk Onderzoek (Netherlands Organization for Scientific Research, NWO). The 2nd author is currently a postdoctoral fellow of the Research Foundation – Flanders (FWO) and is grateful for its financial support (project FWO 12M5319N).

References

[1] Zanforlin S. Advantages of vertical axis tidal turbines set in close proximity: a comparative CFD investigation in the English channel. Ocean Eng 2018;156:358–72.

[2] Tummala A, Velamati RK, Sinha DK, Indraja V, Krishna VH. A review on small scale wind turbines. Renew Sustain Energy Rev 2016;56:1351–71.

[3] Carbó Molina A, De Troyer T, Massai T, Vergaerde A, Runacres MC, Bartoli G. Effect of turbulence on the performance of VAWTs: an experimental study in two different wind tunnels. J Wind Eng Ind Aerodyn 2019;193:103969.

[4] Vergaerde A, De Troyer T, Carbó Molina A, Standaert L, Runacres MC. Design, manufacturing and validation of a vertical-axis wind turbine setup for wind tunnel tests. J Wind Eng Ind Aerodyn 2019;193:103949.

[5] Rezaeiha A, Montazeri H, Blocken B. A framework for large-scale urban wind energy potential assessment: case study for The Netherlands. 2019. submitted for publication.

[6] Rezaeiha A, Pereira R, Kotsonis M. Fluctuations of angle of attack and lift coefficient and the resultant fatigue loads for a large horizontal axis wind turbine. Renew Energy 2017;114(B):904–16.

[7] Visbal MR, Garmann DJ. Analysis of dynamic stall on a pitching airfoil using high-fidelity large-eddy simulations. AIAA J 2018;56(1):46–63.

[8] Tsai H-C, Colonius T. Coriolis effect on dynamic stall in a vertical axis wind turbine. AIAA J 2016;54(1):216–26.

[9] Bianchini A, Balduzzi F, Ferrara G, Ferrari L. Virtual incidence effect on rotating airfoils in Darrieus wind turbines. Energy Convers Manag 2016;111:329–38.

[10] Snel H. Review of aerodynamics for wind turbines. Wind Energy 2003;6(3):203–11.

[11] Leishman JG. Challenges in modelling the unsteady aerodynamics of wind turbines. Wind Energy 2002;5(2–3):85–132.

[12] Snel H. Review of the present status of rotor aerodynamics. Wind Energy 1998;1:46–69.

[13] Fujisawa N, Shibuya S. Observations of dynamic stall on Darrieus wind turbine blades. J Wind Eng Ind Aerodyn 2001;89:201–14.

[14] Ferreira C, van Kuik G, van Bussel G, Scarano F. Visualization by PIV of dynamic stall on a vertical axis wind turbine. Exp Fluid 2009;46(1):97–108.

[15] Buchner A-J, Soria J, Honnery D, Smits AJ. Dynamic stall in vertical axis wind turbines: scaling and topological considerations. J Fluid Mech 2018;841:746–66.

[16] Melius M, Cal RB, Mulleners K. Dynamic stall of an experimental wind turbine blade. Phys Fluids 2016;28(3):034103.

[17] Hand B, Kelly G, Cashman A. Numerical simulation of a vertical axis wind turbine airfoil experiencing dynamic stall at high Reynolds numbers. Comput Fluid 2017;149:12–30.

[18] Dyachuk E, Goude A, Bernhoff H. Dynamic stall modeling for the conditions of vertical axis wind turbines. AIAA J 2014;52(1):72–81.

[19] Rezaeiha A, Montazeri H, Blocken B. CFD analysis of dynamic stall on vertical axis wind turbines using scale-adaptive simulation (SAS): comparison against URANS and hybrid RANS/LES. Energy Convers Manag 2019;196(C):1282–98.

[20] Mulleners K, Raffel M. The onset of dynamic stall revisited. Exp Fluid 2011;52(3):779–93.

[21] Mulleners K, Raffel M. Dynamic stall development. Exp Fluid 2013;54(2).

[22] Heine B, Mulleners K, Joubert G, Raffel M. Dynamic stall control by passive disturbance generators. AIAA J 2013;51(9):2086–97.

[23] Visbal MR, Benton SI. Exploration of high-frequency control of dynamic stall using large-eddy simulations. AIAA J 2018;56(8):2974–91.

[24] Pape AL, Costes M, Joubert G, David F, Deluc JM. Dynamic stall control using deployable leading-edge vortex generators. AIAA J 2012;50(10):2135–45.

[25] Gad-el-Hak M, Bushnell DM. Separation control: review. J Fluids Eng 1991;113(1):5–30.

[26] Gad-el-Hak M. The art and science of flow control. In: Frontiers in experimental fluid mechanics. Heidelberg: Springer-Verlag Berlin; 1989.

[27] Bushnell DM. Drag reduction in nature. Annu Rev Fluid Mech 1991;23:65–79.

[28] Gad-el-Hak M. Modern developments in flow control. Appl Mech Rev 1996;49:365–79.

[29] Joslin RD. Aircraft laminar flow control. Annu Rev Fluid Mech 1998;30:1–29.

[30] Gad-el-Hak Me. Flow control: fundamentals and practices. Springer Berlin Heidelberg; 1998.

[31] Gad-el-Hak M. Flow control: passive, active, and reactive flow management. Cambridge University Press; 2000.

[32] Bewley TR. Flow control: new challenges for a new Renaissance. Prog Aerosp Sci 2001;37:21–58.

[33] Collis SS, Joslin RD, Seifert A, Theofilis V. Issues in active flow control: theory, control, simulation, and experiment. Prog Aerosp Sci 2004;40(4–5):237–89.

[34] Hansen MOL, Velte CM, Øye S, Hansen R, Sørensen NN, Madsen J, Mikkelsen R. Aerodynamically shaped vortex generators. Wind Energy 2016;19(3):563–7.

[35] Storms BL, Jang CS. Lift enhancement of an airfoil using a Gurney flap and vortex generators. J Aircr 1994;31(3):542–7.

[36] Baldacchino D, Ferreira C, De Tavernier D, Timmer WA, van Bussel GJW. Experimental parameter study for passive vortex generators on a 30% thick airfoil. Wind Energy 2018;21(9):745–65.

[37] Wang JJ, Li YC, Choi KS. Gurney flap—lift enhancement, mechanisms and applications. Prog Aerosp Sci 2008;44(1):22–47.

[38] Cattafesta LN, Sheplak M. Actuators for active flow control. Annu Rev Fluid Mech 2011;43(1):247–72.

[39] Choi H, Jeon W-P, Kim J. Control of flow over a bluff body. Annu Rev Fluid Mech 2008;40(1):113–39.

[40] Barlas TK, van Kuik GAM. Review of state of the art in smart rotor control research for wind turbines. Prog Aerosp Sci 2010;46(1):1–27.

[41] Johnson SJ, Baker JP, van Dam CP, Berg D. An overview of active load control techniques for wind turbines with an emphasis on microtabs. Wind Energy 2010;13(2–3):239–53.

[42] Bieler H. Active flow control concepts and application opportunities. Aircraft Eng Aero Technol 2017;89(5):725–9.

[43] Raiola M, Discetti S, Ianiro A, Samara F, Avallone F, Ragni D. Smart rotors: dynamic-stall load control by means of an actuated flap. AIAA J 2018:1–14.

[44] Shmilovich A, Yadlin Y. Flow control techniques for transport aircraft. AIAA J 2011;49(3):489–502.

[45] Brunet V, Dandois J, Verbeke C. Recent Onera flow control research on high-lift configurations. Aerospace Lab Journal 2013;6:1–12.

[46] Prandtl L. Uber Fliissigkeitsbewegung bei sehr kleiner Reibung. In: Proceeding of third international mathematics congress; 1904. p. 484–91. Heidelberg, Germany.

[47] Johnson SJ, Van Dam CP, Berg DE. Active load control techniques for wind turbines. 2008. Sandia National Laboratories SAND2008-4809.

[48] Zwang L. Boundary layer suction on a horizontal axis wind turbine: an aerodynamic design of a thick airfoil for application, vol. 108. TU Delft; 2009.

[49] Ghedin F. Structural design of a 5 MW wind turbine blade equipped with boundary layer suction technology: analysis and lay-up optimisation applying a promising technology. MSc. TU Delft; 2010.

[50] Piperas AT. Investigation of boundary layer suction on a wind turbine airfoil using CFD. MSc. Wind Energy, DTU; 2010.

[51] de Oliveira G. Wind turbine airfoils with boundary layer suction: a novel design approach. MSc. TU Delft; 2011.

[52] Pechlivanoglou G. Passive and active flow control solutions for wind turbine blades. PhD. TU Berlin; 2013.

[53] Wolf A, Lutz T, Würz W, Krämer E, Stalnov O, Seifert A. Trailing edge noise reduction of wind turbine blades by active flow control. Wind Energy; 2014.

[54] Wang Z, Wang Y, Zhuang M. Improvement of the aerodynamic performance of vertical axis wind turbines with leading-edge serrations and helical blades using CFD and Taguchi method. Energy Convers Manag 2018;177:107–21.

[55] Wang Z, Zhuang M. Leading-edge serrations for performance improvement on a vertical-axis wind turbine at low tip-speed-ratios. Appl Energy 2017;208:1184–97.

[56] Zhu H, Hao W, Li C, Ding Q. Numerical study of effect of solidity on vertical axis wind turbine with Gurney flap. J Wind Eng Ind Aerodyn 2019;186:17–31.

[57] Bianchini A, Balduzzi F, Di Rosa D, Ferrara G. On the use of Gurney Flaps for the aerodynamic performance augmentation of Darrieus wind turbines.

Energy Convers Manag 2019;184:402–15.
[58] Ferreira C, Scheurich F. Demonstrating that power and instantaneous loads are decoupled in a vertical-axis wind turbine. Wind Energy 2014;17(3): 385–96.
[59] Rezaeiha A, Kalkman I, Blocken B. Effect of pitch angle on power performance and aerodynamics of a vertical axis wind turbine. Appl Energy 2017;197: 132–50.
[60] Rezaeiha A, Montazeri H, Blocken B. Towards optimal aerodynamic design of vertical axis wind turbines: impact of solidity and number of blades. Energy 2018;165(B):1129–48.
[61] Greenblatt D, Lautman R. Inboard/outboard plasma actuation on a vertical-axis wind turbine. Renew Energy 2015;83:1147–56.
[62] Xiao Q, Liu W, Incecik A. Flow control for VATT by fixed and oscillating flap. Renew Energy 2013;51:141–52.
[63] Greenblatt D, Schulman M, Ben-Harav A. Vertical axis wind turbine performance enhancement using plasma actuators. Renew Energy 2012;37(1): 345–54.
[64] Sasson B, Greenblatt D. Effect of leading-edge slot blowing on a vertical axis wind turbine. AIAA J 2011;49(9):1932–42.
[65] Rezaeiha A, Kalkman I, Montazeri H, Blocken B. Effect of the shaft on the aerodynamic performance of urban vertical axis wind turbines. Energy Convers Manag 2017;149(C):616–30.
[66] Buchner AJ, Lohry MW, Martinelli L, Soria J, Smits AJ. Dynamic stall in vertical axis wind turbines: comparing experiments and computations. J Wind Eng Ind Aerodyn 2015;146:163–71.
[67] Rezaeiha A, Montazeri H, Blocken B. Towards accurate CFD simulations of vertical axis wind turbines at different tip speed ratios and solidities: guidelines for azimuthal increment, domain size and convergence. Energy Convers Manag 2018;156(C):301–16.
[68] Rezaeiha A, Kalkman I, Blocken B. CFD simulation of a vertical axis wind turbine operating at a moderate tip speed ratio: guidelines for minimum domain size and azimuthal increment. Renew Energy 2017;107:373–85.
[69] Rezaeiha A, Montazeri H, Blocken B. On the accuracy of turbulence models for CFD simulations of vertical axis wind turbines. Energy 2019;180(C):838–57.
[70] Blocken B, Stathopoulos T, Carmeliet J. Wind environmental conditions in passages between two long narrow perpendicular buildings. J Aerosp Eng 2008;21(4):280–7.
[71] Rezaeiha A, Montazeri H, Blocken B. Characterization of aerodynamic performance of vertical axis wind turbines: impact of operational parameters. Energy Convers Manag 2018;169(C):45–77.
[72] van der Hoeven T. Slot suction of the turbulent boundary layer: an experimental study. Delft, The Netherlands: Faculty of Aerospace Engineering, TU Delft; 2013.
[73] Drela M. XFOIL: an analysis and design system for low Reynolds number airfoils. In: Low Reynolds number aerodynamics: vol. 54 of the series 'lecture notes in engineering'. Springer; 1989. p. 1–12.
[74] Lee T, Gerontakos P. Investigation of flow over an oscillating airfoil. J Fluid Mech 2004;512:313–41.
[75] Pierpont PK. Investigation of suction-slot shapes for controlling a turbulent boundary layer. 1974. NASA Technical Note No. 1292, Washington, USA.
[76] Fage A, Sargent RF. Design of suction slots. 1944. Aeronatical Research Council (ARC) Report No. 2127, London, UK.
[77] KNF micro- and mini-pumps for air and gas: https://www.knfusa.com/en/micro-air/.